Noname manuscript No.
(will be inserted by the editor)

Further Probing the Mechanisms Driving Projected Decreases of Extreme Precipitation Intensity over the Subtropical Atlantic

M. A. Thabo Mpanza · Neil F. Tandon

Received: date / Accepted: date

Abstract Regional projections of extreme precipitation intensity (EPI) are strongly influenced by changes of "extreme ascent," i.e. ascending air during periods of extreme precipitation. Earlier studies have suggested that long-term changes in eddy length scale and vertical stability are key factors influencing extreme ascent projections, but these mechanisms have yet to be confirmed with controlled model experiments. In this study, we perform such controlled experiments using a cloud-resolving model (CRM). The selected CRM domains are three locations over the subtropical Atlantic Ocean where global climate models consistently project weakening of extreme ascent with accordingly decreased EPI. At each study location, four to ten pairs of 20-year-maximum precipitation events are simulated with the CRM, with

M. A. Thabo Mpanza
York University
4700 Keele St.
Toronto, ON M3J 1P3
Canada
Tel.: +14167362100 ext. 40053
Fax: +14167365817
E-mail: thabomp1@yorku.ca
On leave from:
South African Weather Service

N. F. Tandon
York University

each pair consisting of an event during the historical period (1981-2000) and an event during the future period (2081-2100). Large-scale forcings for these events are derived from members of an initial condition ensemble of the Canadian Earth System Model version 2 (CanESM2). These experiments reveal that, in all three study locations, weakening of differential cyclonic vorticity advection (dCVA) is a key driver of projected decreases in extreme ascent and EPI. Possible mechanisms responsible for weakening dCVA are discussed. Although there is evidence that EPI in the CRM has different sensitivity to large-scale forcings than CanESM2, the role of dCVA changes may nonetheless be important to consider for EPI changes in the real world.

Keywords extreme precipitation · atmospheric dynamics · climate change · future projections · cloud-resolving model · climate model

1 Introduction

Extreme precipitation events (EPEs) often have devastating effects on communities and livelihoods. The World Meteorological Organization (WMO) recognizes two standard definitions of extreme precipitation: (1) when precipitation exceeds a fixed threshold that is associated with a certain level of impact, and (2) when precipitation exceeds a relative threshold based on return period or percentile in a given region (WMO, 2018). Regardless of the precise definition used, EPEs can damage infrastructure, endanger food security and inflict loss of human life (Masson-Delmotte et al, 2018).

Extreme precipitation led to the Alberta floods of 2013, which affected approximately 100,000 people in 29 jurisdictions and incurred approximately C$5-6 billion in damages, making it the second costliest disaster in Canadian history (Milrad et al, 2017). The Pakistan floods of 2010 resulted in over 1900 fatalities and damaged over a million homes. The World Bank estimated that this disaster cost US$9.7 billion in damages (Vaqar et al, 2011; Kronstadt et al, 2011). The record-breaking Texas floods of May 2015 resulted from the highest 5-day precipitation accumulations over that region in 68 years (Nie et al, 2018).

The cases highlighted above are just a few of many examples of EPEs in different regions around the world, and there is a great need to provide reliable projections of how the intensity of such EPEs will change in the future. In a warmer climate, the available moisture in the atmosphere is expected to increase in accordance with the Clausius-Clapeyron relation, resulting in increased intensity of both mean and extreme precipitation intensity over most regions (Trenberth, 1999; Trenberth et al, 2015).

However, this simple thermodynamic explanation fails to explain many aspects of the observational record in particular regions. Observations of extreme precipitation show that, over recent decades, the intensity of such events is increasing more rapidly than regional mean precipitation in most regions (Bao et al, 2017; Pfahl et al, 2017). Intriguingly, observations show regions where mean precipitation trends are negative but trends of extreme precipitation intensity (EPI) are positive (Alexander et al, 2006). Furthermore, there is large spatial variability in observed EPI trends, ranging from 0% K^{-1} at 13°S and 11°N to above 10% K^{-1} at the equator and high latitudes when EPI events are zonally aggregated (Westra et al, 2013), and there are some regions where EPI trends are negative (Alexander et al, 2006). There is also large seasonal variability in EPI trends. Zheng et al (2015) analyzed Australian rain gauge data over 1966-2012 and showed that EPI has increased significantly during summer but decreased during fall.

Global climate models (GCMs) have been crucial to untangling the physical processes responsible for extreme precipitation. Pfahl et al (2017) analyzed 22 models participating in the Coupled Model Intercomparison Project Phase 5 (CMIP5) and compared model output during the historical period against the Global Precipitation Climatology Project (GPCP) dataset. GPCP is a blend of quality-controlled rain gauge, satellite and sounding rainfall data (Huffman et al, 1997). In general, the simulated spatial pattern of EPEs agrees well with observations, but quantitatively, simulated EPI shows some high bias in East Asia and tropical-to-southern Africa and some low bias over the Americas. Models generally produce stronger EPI over oceans compared to GPCP, but there are no ground measurements to constrain GPCP over oceans, rendering such a comparison inconclusive. Some quantitative difference

between models and observations is expected since EPEs typically occur in small-scale convective clusters and such clusters are not resolved in GCMs. On the other hand, spatial patterns of EPEs are also often associated with large-scale circulation patterns, which GCMs do resolve.

Of particular interest are the future projections of GCMs. In line with thermodynamic expectations, both simplified and comprehensive GCMs project increased EPI over most of the globe (O'Gorman and Schneider, 2009a; O'Gorman and Schneider, 2009b; Pendergrass et al, 2015, 2016; Pfahl et al, 2017). However, in some regions, long-term decreases in EPI are projected. This regional variability has been linked to regional variations in projections of vertical velocity during EPEs (Pfahl et al, 2017; Tandon et al, 2018a), referred to as "extreme ascent." The contribution of extreme ascent to EPI is often referred to as the "dynamical component" of EPI.

In addition to the regional variability of EPI projections, Pfahl et al (2017) have shown that the pattern and magnitude of the dynamical component is very different during summer than during winter. For this reason, climate change might also influence the seasonal cycle of extreme precipitation. Results of several studies indicate a possible global shift in the seasonality of extreme precipitation towards colder seasons (Rajczak et al, 2013; Pfahl et al, 2017; Brönnimann et al, 2018; Marelle et al, 2018). Because of strong seasonal variations in soil moisture and snow melt, changes in extreme precipitation seasonality can greatly exacerbate flood risk (Marelle et al, 2018). For this reason, changes in extreme precipitation seasonality can have serious consequences for various sectors such as agriculture, tourism, property insurance, hydroelectric power and water resources.

Earlier studies have performed analysis suggesting that long-term changes in the horizontal scale of vertical velocity anomalies, referred to as "eddy length," are a key factor influencing regional extreme ascent projections (Tandon et al, 2018a,b). Projected increases in eddy length are expected to weaken the coupling between convection and the large-scale vertical velocity, which in turn weakens extreme ascent, thereby reducing the precipitation intensity. (This mechanism is discussed in greater detail in section 2.) These findings were based on analysis of output from state-of-the-art fully coupled GCMs. Other studies have argued that changes in vertical

stability are a key factor influencing extreme ascent projections (Nie et al, 2020; Li and O'Gorman, 2020). To some extent, these mechanisms are related because eddy length depends on vertical stability, and eddy length is expected to change as a result of long-term changes in vertical stability (Kidston et al, 2010; Tandon et al, 2018b).

Despite the valuable insights gained from GCMs, understanding regional processes that lead to EPE changes is challenging due to the complexity of the models and unresolved processes. Thermodynamic and dynamical coupling between adjacent atmospheric grid cells, as well as coupling between the atmosphere and the surface, makes it difficult to isolate mechanisms responsible for the projected EPI changes. Furthermore, while GCMs are capable of capturing the long-term statistics of many EPEs (Randall et al, 2007; Pierce et al, 2009), they are limited in their ability to simulate individual EPEs in the observational record, as the precise initialization and pre-conditioning required is typically not attainable with a GCMs limited spatial and temporal resolutions. Finer resolution regional models allow for controlled experimentation that can more easily isolate physical mechanisms relevant to extreme ascent in both observations and GCMs (Nie and Sobel, 2016; Nie et al, 2016b, 2018).

In this study, a dynamical downscaling approach is implemented using a cloud-resolving model (CRM) over a limited domain approximately corresponding to a single GCM grid box. This modelling framework captures coupling between convection and the large-scale circulation (Nie and Sobel, 2016; Nie et al, 2018) while retaining control over the large-scale forcings being applied to the CRM domain (i.e. eddy length, stability and horizontal advection). This approach is complementary to the approach commonly used in previous studies, which simulate extreme precipitation in continental-scale regional models (e.g., Prein et al, 2016; Liu et al, 2017; Coppola et al, 2020; Hegdahl et al, 2020; Pichelli et al, 2021). Such models can better capture mesoscale convective development, but they allow less control over the large-scale forcings and their coupling to convection in localized regions. In our modelling framework, we can perturb large-scale forcings in such a way as to gain insight into the key processes responsible for changes in EPI in localized regions. Insights gained from such experiments can in turn motivate further improvements in GCM parameterizations, thereby improving confidence in model projections of EPI.

In this study, we focus on subtropical regions where dynamical effects are expected to drive long-term decreases in EPI (Pfahl et al, 2017; Tandon et al, 2018b; Nie et al, 2020). Improved understanding of such dynamical effects will lead to greater understanding of less dominant (but still important) dynamical effects in other regions over both land and ocean. In contrast with earlier studies, our experiments suggest that changes in differential vorticity advection (VA) are the dominant driver of projected subtropical decreases in EPI. (Section 2 discusses differential VA in more detail so as to make intuitive sense of its influence on EPI.)

This paper is organized as follows: In Section 2, we provide some additional theoretical background for understanding changes in extreme ascent. Methods are explained in section 3, including description of the modelling framework, forcing dataset and experimental design. In section 4, we present and discuss the results of our CRM experiments. Section 5 provides a summary of the key results and concluding remarks.

2 The Quasigeostrophic Omega Equation

Complementary to various numerical modelling tools, the quasigeostrophic omega (QGω) equation provides an especially useful framework for analyzing mechanisms relevant for extreme ascent. The QGω equation combines the quasigeostrophic vorticity, thermodynamic and continuity equations into a form that allows computation of the vertical pressure velocity, ω, from the instantaneous three-dimensional geostrophic flow field (Holton and Hakim, 2012). The QGω equation, including a diabatic forcing term, can be written as

$$\partial_{pp}\omega + \frac{\sigma}{f_0^2}\nabla^2\omega = -\frac{1}{f_0}\partial_p \mathrm{Adv}(\zeta) - \frac{R}{pf_0^2}\nabla^2 \mathrm{Adv}(T) - \frac{R}{pf_0^2}\nabla^2 Q, \tag{1}$$

where p is pressure, σ is the dry static stability, f_0 is the reference value of the Coriolis parameter (f), ∇^2 is the horizontal Laplacian operator, R is the gas constant for dry air, ζ is the geostrophic absolute vorticity, T is temperature and Q is the diabatic heating. The horizontal geostrophic advection operator is defined as

$$\mathrm{Adv}(\cdot) \equiv -u_g\partial_x(\cdot) - v_g\partial_y(\cdot), \tag{2}$$

where u_g and v_g are the horizontal geostrophic winds in the x (zonal) and y (meridional) directions, respectively. The dry stability is given by $\sigma = -(RT/p)\partial_p \ln\theta$, where θ is potential temperature. The geostrophic vorticity is given by

$$\zeta = \frac{1}{f_0}\nabla^2\phi + f, \tag{3}$$

where ϕ is the geopotential.

The horizontal and vertical curvature of ω will typically be opposite in sign to ω. (Consider, for example, a vertical velocity anomaly that is localized in the horizontal, and parabolic over the depth of the troposphere.) Thus, for ascending motion ($\omega < 0$), the left-hand side (LHS) of (1) is positive. One key effect of the Laplacian is that ω responds to spatially averaged gradients of the forcing terms rather than localized gradients.

The QGω equation has three forcing terms on its right-hand side (RHS). The first forcing term is the differential VA. When VA is increasing with height [$\partial_p \mathrm{Adv}(\zeta) < 0$], referred to as differential cyclonic vorticity advection (dCVA), that implies that at a given location, the relative vorticity is increasing more rapidly with time at higher levels compared to lower levels, which implies that the curvature of height surfaces is more rapidly increasing with time at higher levels than at lower levels. This in turn implies that height levels are getting closer in pressure, which in the absence of other forcings implies ascending motion ($\omega < 0$). This physically intuitive result is mathematically clear from (1) for $\partial_p \mathrm{Adv}(\zeta) < 0$.

The second term on the RHS of (1) is the Laplacian of temperature advection (TA). If there is warm air advection [$\mathrm{Adv}(T) > 0$] that is spatially localized, then $\nabla^2 \mathrm{Adv}(T) < 0$, which in the absence of other forcings implies $\omega < 0$. The last term on the RHS is the diabatic heating term, which is primarily convective heating on the time scales of an EPE. If the convective heating anomaly is positive and localized, then $\nabla^2 Q < 0$, so convective heating will force upward motion. On the LHS of (1), the key parameter is static stability (σ). For a given positive forcing, smaller values of σ imply a less stable atmosphere and accordingly larger (more negative) values of ω.

The QGω equation is typically applied in the midlatitudes, where the underlying scaling arguments of QG theory are most justifiable. However, it can be shown (see Nie and Sobel, 2016) that as f_0 approaches zero, the horizontal advection terms become small as well, and the QGω equation reduces to the weak temperature gradient approximation (Sobel and Bretherton, 2000). On this basis, it is reasonable to apply the QGω equation in the tropics as well, although numerical schemes may become unstable within a few degrees of the equator (e.g. Li and O'Gorman, 2020). Furthermore, Li and O'Gorman (2020) have shown that poleward of 7° latitude, extreme ascent in GCMs during EPEs can be closely approximated by numerically solving the QGω equation. It is therefore reasonable to apply the QGω equation to understanding EPEs in the subtropics, which are the focus of this study.

The QGω equation can be solved numerically with just a single forcing term from the RHS of (1) to obtain the particular ω solution associated with that forcing. Because the QGω equation is linear, the total ω solution is just the sum of the three particular solutions, i.e.

$$\omega = \omega_\zeta + \omega_T + \omega_Q, \tag{4}$$

where ω_ζ is the solution with only differential VA forcing applied, ω_T is the solution with only TA forcing applied and ω_Q is the solution with only diabatic forcing applied (Nie and Sobel, 2016).

Assuming ω has wavelike structure with horizontal length scale L (where L is an inverse wavenumber), then the Laplacian in (1) can be replaced by $-1/L^2$, yielding

$$\partial_{pp}\omega_E - \frac{\sigma\omega_E}{f_0^2 L_E^2} = -\frac{1}{f_0}\partial_p \mathrm{Adv}(\zeta_E) + \frac{R}{p f_0^2 L_E^2}\mathrm{Adv}(T_E) + \frac{RQ_E}{p f_0^2 L_E^2}. \tag{5}$$

Here, the subscript E indicates values computed on days of extreme precipitation, which is our focus in this study. Nie and Sobel (2016) performed scaling analysis of this equation and showed that the Rossby radius of deformation ($L_R = \Pi\sqrt{\sigma}/f_0$, where Π is a representative vertical pressure scale of motion) provides a useful scale against which to determine the dominant balances in (5). Such analysis reveals that for large eddy lengths ($L_E > L_R$), the dominant balance is between the first term on the LHS and the first term on the RHS, reflecting a state in which the large-scale circulation is decoupled from convection and vertical velocity is determined

entirely by differential VA. In such a regime, we expect an increase in eddy length to increase the advective time scale of a precipitating weather system, thus increasing the accumulated precipitation (e.g., Dwyer and O'Gorman, 2017).

Conversely, for small eddy lengths ($L_E < L_R$), convection and the large-scale circulation are strongly coupled, and the dominant balance is between adiabatic ascent, temperature advection and diabatic heating (Nie and Sobel, 2016). Tandon et al (2018b) have presented evidence suggesting that GCM-projected changes in subtropical extreme ascent are mostly driven by changes in diabatic heating, in accordance with the fact that subtropical L_E is small compared to L_R, suggesting that contributions from differential VA are weak. In such a regime, we expect an increase in eddy length to reduce coupling between convection and the large scale circulation, thus reducing the strength of extreme ascent. In other words, the influence of eddy length on precipitation depends on the degree of coupling between convection and the large-scale circulation. In the strongly-coupled regime, we expect an L_E increase to decrease EPI, and in the weakly-coupled regime, we expect an L_E increase to increase EPI.

3 Data and Methodology

3.1 Cloud resolving model configuration

Our experiments utilize the column quasigeostrophic (CQG) framework, which relies on the QGω equation for wave-like disturbances (equation 5). In this formulation, coupling between convection and the large-scale vertical velocity is parameterized in terms of the eddy length (L) of the large-scale vertical velocity, as schematically depicted in Fig. 1.

In this study, the CQG framework is implemented in a specific CRM called the System for Atmospheric Modeling (SAM) (Khairoutdinov and Randall, 2003) with the details of the implementation described in Nie et al (2018). SAM is a non-hydrostatic anelastic model, and we run it with a timestep of 10 s over a 128 km by 128 km domain with 2 km horizontal resolution and doubly periodic lateral bound-

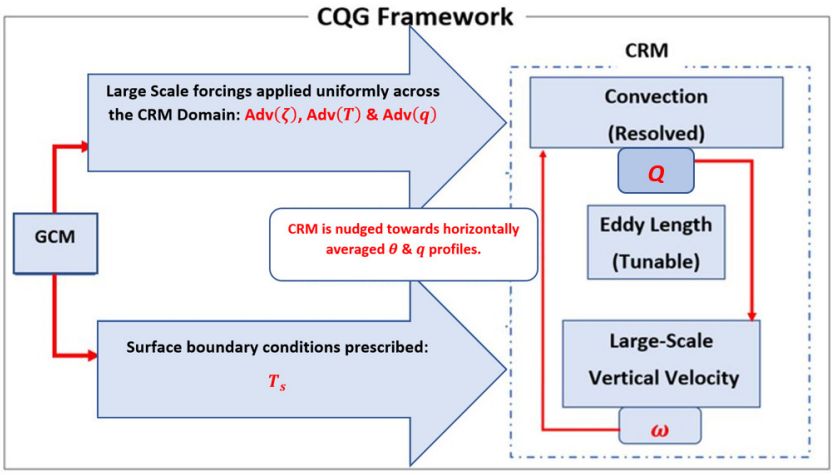

Fig. 1 Schematic diagram of the column quasigeostrophic (CQG) framework used in this study.

aries. At such resolution, the CRM explicitly resolves convection within the domain. The model has 64 vertical levels with spacing ranging from 75 m near the surface to 500 m in the free troposphere.

The domain size we use would not capture the development of organized convective systems over larger regions, which might be important for observed EPEs. In this study, however, we are primarily concerned with understanding EPI mechanisms in GCMs, which do not capture organized convective systems. Thus, the domain size used in this study is appropriate for examining EPI mechanisms in GCMs.

At each time step, the horizontally averaged diabatic heating produced by the CRM is fed into the QGω equation along with imposed horizontal advection of temperature and absolute vorticity taken from a GCM. (The GCM forcing data are described in more detail below.) These large-scale forcings are applied evenly across the CRM domain. The QGω equation is then solved for the large-scale vertical velocity, which is used to compute large-scale temperature and moisture tendencies at every level, which are fed back into the CRM. In this way, the CRM captures coupling between convection and the large-scale vertical velocity.

Insolation in the CRM varies with the diurnal cycle, but the daily mean insolation is held fixed to its daily mean value at the beginning of the simulation period. (We performed tests with seasonally varying insolation, and our results were not affected.)

Surface temperature, T_s, is prescribed. Horizontally averaged potential temperature and moisture are nudged toward prescribed GCM-derived time-varying vertical profiles of temperature and specific humidity, with a nudging timescale of six hours. Fully interactive radiation is applied within the CRM, updating at every model time step. For the CRM radiation scheme, we use the same ozone profile as is used in the driving GCM, corresponding to the average ozone concentration over the month during which the simulated EPE occurs.

3.2 CanESM2 forcing data

SAM is forced with large scale temperature, moisture, geopotential height and wind fields derived from output of the Canadian Earth System Model version 2 (CanESM2, Arora et al, 2011). CanESM2 is a fully-coupled earth system model developed by the Canadian Centre for Climate Modelling and Analysis (CCCma). The atmospheric component of CanESM2 is a spectral model employing T63 triangular truncation, corresponding to approximately $2.8^\circ \times 2.8^\circ$ horizontal resolution, with 35 vertical levels.

The CanESM2 output came from a 50-member ensemble simulating the historical (1950-2005) and future (2006-2100) periods. The future portion of the simulation follows the high-emission representative concentration pathway 8.5 (RCP8.5) scenario. RCP8.5 combines assumptions about high population growth and modest technological improvement in the absence of climate change mitigation policy, leading to high greenhouse gas (GHG) emissions (Riahi et al, 2011). This CanESM2 ensemble was generated from five historical runs initialized in 1850, each of which was branched in 1950 into ten ensemble members obtained by applying perturbations to the initial atmospheric state. Thus, this large ensemble samples five different ocean initial states and fifty different atmospheric initial states. In the model output archive, these ensemble members are organized into five "ensemble groups" labelled r1 through r5, corresponding to each of the five historical runs initialized in 1850, and within each of these ensemble groups, the ten atmosphere-perturbed runs are labelled r1 through r10. Taking an ensemble approach helps with separating "externally forced" changes

(i.e. changes due to increased greenhouse gases) from internal variability. We use output from only one GCM (CanESM2) both because of the large number of ensemble members available and the availability of all required output variables. Future work will assess whether the mechanisms we identify are at work in other GCMs.

The specific CanESM2 output fields used to force the CRM forcing are as follows: Monthly mean surface air temperature is used for the prescribed surface temperature. Daily and 6-hourly output of air temperature (T), wind (u), specific humidity (q) and geopotential height (ϕ/g, where g is the acceleration due to gravity) are used. The 6-hourly data are archived on model sigma levels, and these are linearly interpolated to pressure levels required by the CRM. Following Nie and Sobel (2016), we use 6-hourly output to compute the horizontal advective forcings required by the CRM. These advective forcings include QG VA [Adv(ζ)], TA [Adv(T)] and moisture advection [Adv(q)]. Even though moisture advection does not appear in the QGω equation (1), it can influence EPI by modifying the amount of moisture in a given column.

Daily CanESM2 output is used to construct vertical profiles of potential temperature and moisture, which are additional large-scale forcings required by the CRM. All time-varying forcings are supplied to the CRM at the same temporal resolution as the CanESM2 output, and the CRM linearly interpolates these forcings in time. The surface boundary condition is prescribed as the seasonal mean of monthly surface air temperature, averaged over the 20-year epoch of interest (1981-2000 for the historical period and 2081-2100 for the future period). Here, the long-term seasonal average is taken including only the month containing the EPE of interest. We have also tested running the CRM with daily varying SST corresponding to the precise dates surrounding the EPE, and our results were not substantially different.

3.3 Eddy length calculation

Eddy length is computed from CanESM2 output following essentially the same procedure as in Tandon et al (2018a,b):

1. On a given day of extreme precipitation at location (x,y), we compute the anomaly of daily mean ω at 500 hPa with respect to the monthly climatology during the relevant epoch.
2. We then compute the zonal and meridional e-folding distances of this ω anomaly relative to (x,y), applying linear interpolation between grid point centres.
3. We divide the e-folding distances by $0.19 \times 2\pi$ to obtain the zonal and meridional scales of the corresponding waves, L_x and L_y respectively, expressed as inverse wavenumbers. As shown by Barnes and Hartmann (2012), this factor arises from the fact that the e-folding distance of a cosine wave is 0.19 times its wavelength.
4. We combine L_x and L_y to obtain an effective eddy length, $L_E = (L_x^{-2} + L_y^{-2})^{-1/2}$.
5. We multiply L_E by an adjustment factor in order to maintain the numerical stability of the CRM. [This step was not taken by Tandon et al (2018a,b), and we provide further explaination below.]

The second-last step in this procedure is a refinement of the procedure used in Tandon et al (2018a,b), who use $L_E = \sqrt{L_x^2 + L_y^2}$. While the latter is a heuristically reasonable approach, it is not mathematically consistent with how zonal and meridional wavenumbers are typically combined. The approach used in this study produces L_E values that are lower by a factor of approximately two compared to the values obtained by Tandon et al (2018a,b).

Different methods have been suggested for computing eddy length relevant for the QGω equation. For example, Dai and Nie (2020) compute eddy length based on geopotential height anomalies, and they obtain results that are larger than the eddy lengths computed from the ω field. Our argument for computing eddy length based on the ω field is that ω is the field being solved for in the QGω equation (5). The assumption that solutions to the QGω equation have wavelike structure means that the eddy length on the LHS of equation (5) corresponds to the ω field. It is also reasonable to assume, as we do, that the forcing terms have the same eddy length as ω, in which case the eddy lengths on the LHS and RHS of (5) are equal. Alternatively, one can allow for the possibility that the forcing terms have different eddy lengths from ω (e.g., Li and O'Gorman, 2020). Furthermore, Li and O'Gorman (2020) have

shown that, away from the equator, there is close correspondence between ω obtained directly from model output and the QG ascent computed by inverting the QGω equation. Thus, we do not expect that the eddy length computed directly from model output ω would be different from eddy length computed from QG ω.

To give an example of the eddy length computation, for one CanESM2 ensemble member at one of our study locations (26.51°S, 2.83°W), we obtained $L_{E0} = 227$ km during the historical period, and we obtained $L_E = 456$ km during the future period. (We use the "0" subscript hereafter when referring to values during the historical period.) We attempted to prescribe these eddy length values in the CRM, but such small horizontal eddy lengths created numerical instability in the CRM owing to unrealistically strong updrafts. Such numerical instability is not surprising, as CanESM2 parameterizes convection, and sensitivity of the GCM convection scheme to large-scale forcing may be very different to the sensitivity of a CRM to the same large-scale forcing.

In order for the CRM to run without numerical instability, we increase the eddy length compared to its CanESM2-derived value. This adjustment factor ranges from 2.1 to 6.6, and it is applied to both the historical and future L_E values so that $\delta L_E^2/L_{E0}^2$ in the CRM runs matches $\delta L_E^2/L_{E0}^2$ in the GCM runs. (We use δ hereafter when referring to "climatic changes" between the historical and future periods.) The specific adjustment factor for each experiment is provided in Table 1. Such adjustment factors might result in EPEs whose mechanisms are different in the CRM compared to the GCM. We are planning to perform additional experiments using a convection-parameterizing single column model to examine this possibility. On the other hand, it is possible that the eddy lengths in CanESM2 are unrealistically small, as they are much smaller than a Rossby radius (order 1000 km), which is the expected horizontal scale for synoptic systems. Indeed, some of the CanESM2 EPEs investigated in this study have spatial scales that are close to the spatial resolution of CanESM2, calling their realism into question, and it possible that the eddy length adjustment factors we apply result in more realistic behaviour, with eddy lengths more in line with the Rossby radius.

3.4 Model experiments

We have constructed specific CRM experiments based on the results of Tandon et al (2018b), who have examined regional variability of extreme precipitation projections in the CanESM2 large ensemble. Fig. 2a shows the CanESM2-derived composite climatic change of the 20-year maximum of daily precipitation ($\delta P_E / P_{E0}$), normalized by the zonal mean climatic change of annual mean surface temperature. Fig. 2b shows the dynamical part of the EPI change, isolated by linearly decomposing changes in the vertical moisture advection and isolating a term associated with changes in extreme ascent. [See Tandon et al (2018b) and references therein for details.] As mentioned earlier, there are widespread regions of projected weakening of extreme ascent, especially in the subtropics.

We have chosen three locations in the subtropical Atlantic as our study locations (Fig. 2b). These are locations where weakening of extreme ascent is especially strong, providing some confidence that a clear mechanism will emerge in these locations. Two of these locations are approximately in the centers of the subtropical dry zones in the North and South Atlantic, whereas the third location is closer to the southern edge of the subtropics in the South Atlantic. The two locations in the South Atlantic were chosen in order to assess whether different mechanisms were at work at the edge of the subtropics compared to the middle of the subtropics. Because all three of these locations are over ocean, we also avoid possible complications of land surface interactions. This approach allows us to build up our basic knowledge of mechanisms in a simpler physical setting, which will help inform future investigations of EPE mechanisms over land regions.

Our three study locations are labelled "SA" (26.5107°S, 2.8125°W, black diamond in Fig. 2b), "SAC" (18.1389°S, 19.6875°W, black circle in Fig. 2b), and "NA" (18.14°N, 26.25°W, black square in Fig. 2b). At each of these locations, we have selected four to ten members of the CanESM2 ensemble which show projected decreases in 20-year maximum EPI. Given the effort involved in setting up each CRM experiment, the number of CRM experiments is limited compared to the size of the CanESM2 ensemble. Rather than relying on many CRM experiments to filter out

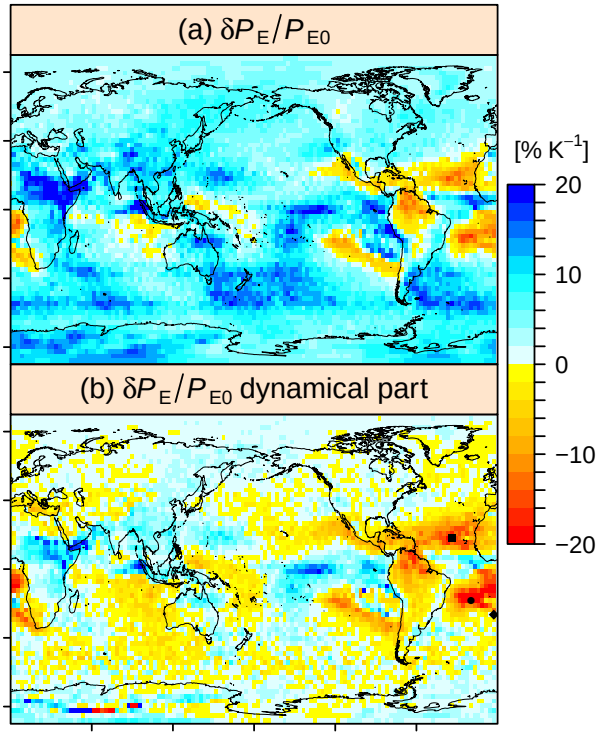

Fig. 2 (a) Composite climatic change in 20-year maximum of daily precipitation and (b) its dynamical part normalized by the zonal mean climatic change in surface temperature, computed from the CanESM2 large ensemble. The black polygons indicate the locations used for the dynamical downscaling experiments in the current study. The square corresponds to the "NA" study location, the circle corresponds to the "SAC" study location and the diamond corresponds to the "SA" study location.

internal variability, we have selected CanESM2 ensemble members whose EPI projections resemble the ensemble mean projections (i.e. projected decreases of EPI and projected increases of eddy length), thus requiring fewer CRM experiments to produce clear results. There was no clear change in the seasonality of EPEs at our study locations, but for some ensemble members the historical and future EPEs occur in different seasons. To avoid potential confounding effects due to such seasonality changes, we only used CanESM2 ensemble members for which the historical and future events occur during the same season, requiring that the calendar months of the historical and future events differ by no more than two. Furthermore, some CanESM2 ensemble members were not usable because the forcings generated from them caused

the CRM to crash. The reason for these crashes require further investigation, but it may relate to the CRM having higher sensitivity to large-scale forcing compared to CanESM2 (a matter discussed further below).

To summarize, we have performed CRM experiments using all CanESM2 runs whose 20-year maximum precipitation during the historical and future periods satisfy all of the following criteria in the study locations:

1. the projected EPE decreases;
2. the projected eddy length increases;
3. the future EPE occurs during the same season as the historical EPE;
4. the associated large-scale forcings do not cause the CRM to crash.

The number of CanESM2 runs that satisfied all of these criteria was 10 over SA, 6 over SAC and 4 over NA. CRM crashes are the main reason why the number of runs over NA is lower than for other study locations: over NA, there were 9 runs satisfying conditions 1-3 above, but the CRM remained numerically stable for only 4 of those runs. CRM crashes did not reduce the number of usable runs over SAC. Instead, the reason there were fewer usable runs over SAC might be due to the fact that EPI was lower over this location compared to the other study locations, resulting in a lower signal-to-noise ratio, thereby reducing the number of runs satisfying conditions 1-3.

Table 1 describes the CanESM2 EPEs examined with our CRM experiments. Case names are constructed starting with the study location name (e.g. SA, SAC or NA), followed by the epoch ("Hist" for historical, "Fut" for future). "GCM" is appended to the case name when examining CanESM2 output directly; otherwise it is assumed that the case is a CRM experiment driven by an ensemble member of CanESM2. Most of our discussion focuses on ensemble averages, but when referring to an individual ensemble member, we refer to it by the ensemble group number followed by the ensemble member number (e.g., "r1r3" for ensemble group 1, ensemble member 3).

To visualize our case selection process, Figs. 3-5 show timeseries of annual maximum daily precipitation from CanESM2 over the three selected locations during the historical (black) and future (red) periods. Included in these figures are all CanESM2

Table 1 Descriptions of the GCM (CanESM2) simulations examined in this study. The eddy length adjustment factor is applied to the GCM-diagnosed eddy length in order to maintain numerical stability of the CRM. See text for additional details.

Case Name	Ensemble Group	Ensemble Member	Location	20-Year Max EPE Date	Eddy Length [km]	Eddy Length Adjustment Factor
SA-Hist-GCM	r1	r3	26.51°S, 2.83°W	22 June 1985	227	3.2
SA-Fut-GCM	r1	r3	26.51°S, 2.83°W	27 July 2091	456	3.2
SA-Hist-GCM	r1	r9	26.51°S, 2.83°W	14 July 1983	476	2.2
SA-Fut-GCM	r1	r9	26.51°S, 2.83°W	15 August 2083	582	2.2
SA-Hist-GCM	r2	r6	26.51°S, 2.83°W	10 May 1985	388	2.7
SA-Fut-GCM	r2	r6	26.51°S, 2.83°W	27 May 2096	399	2.7
SA-Hist-GCM	r2	r10	26.51°S, 2.83°W	13 May 1986	349	3.4
SA-Fut-GCM	r2	r10	26.51°S, 2.83°W	26 May 2087	424	3.4
SA-Hist-GCM	r3	r5	26.51°S, 2.83°W	6 June 1991	319	3.2
SA-Fut-GCM	r3	r5	26.51°S, 2.83°W	21 April 2100	530	3.2
SA-Hist-GCM	r3	r8	26.51°S, 2.83°W	17 May 1998	234	4.4
SA-Fut-GCM	r3	r8	26.51°S, 2.83°W	28 April 2081	684	4.4
SA-Hist-GCM	r3	r10	26.51°S, 2.83°W	16 May 1992	336	2.1
SA-Fut-GCM	r3	r10	26.51°S, 2.83°W	24 May 2093	416	2.1
SA-Hist-GCM	r4	r7	26.51°S, 2.83°W	2 June 1983	397	2.4
SA-Fut-GCM	r4	r7	26.51°S, 2.83°W	24 May 2086	743	2.4
SA-Hist-GCM	r4	r9	26.51°S, 2.83°W	21 May 2000	284	3.6
SA-Fut-GCM	r4	r9	26.51°S, 2.83°W	27 April 2088	290	3.6
SA-Hist-GCM	r5	r7	26.51°S, 2.83°W	1 July 1998	354	2.9
SA-Fut-GCM	r5	r7	26.51°S, 2.83°W	23 June 2098	377	2.9
SAC-Hist-GCM	r1	r10	18.14°S, 19.96°W	15 June 1998	317	3.0
SAC-Fut-GCM	r1	r10	18.14°S, 19.96°W	20 May 2092	472	3.0
SAC-Hist-GCM	r2	r3	18.14°S, 19.96°W	23 July 1987	351	3.4
SAC-Fut-GCM	r2	r3	18.14°S, 19.96°W	13 May 2089	471	3.4
SAC-Hist-GCM	r3	r7	18.14°S, 19.96°W	14 June 1984	200	5.2
SAC-Fut-GCM	r3	r7	18.14°S, 19.96°W	12 June 2081	466	5.2
SAC-Hist-GCM	r3	r8	18.14°S, 19.96°W	29 May 1983	221	4.7
SAC-Fut-GCM	r3	r8	18.14°S, 19.96°W	30 June 2096	292	4.7
SAC-Hist-GCM	r3	r9	18.14°S, 19.96°W	11 March 2000	236	4.4
SAC-Fut-GCM	r3	r9	18.14°S, 19.96°W	18 May 2095	293	4.4
SAC-Hist-GCM	r5	r9	18.14°S, 19.96°W	20 May 1995	423	2.4
SAC-Fut-GCM	r5	r9	18.14°S, 19.96°W	14 May 2092	468	2.4
NA-Hist-GCM	r3	r1	18.14°N, 26.25°W	12 September 1999	225	4.6
NA-Fut-GCM	r3	r1	18.14°N, 26.25°W	14 October 2086	328	4.6
NA-Hist-GCM	r3	r6	18.14°N, 26.25°W	28 October 1990	229	6.6
NA-Fut-GCM	r3	r6	18.14°N, 26.25°W	18 September 2093	308	6.6
NA-Hist-GCM	r4	r6	18.14°N, 26.25°W	16 December 1986	705	2.5
NA-Fut-GCM	r4	r6	18.14°N, 26.25°W	26 December 2095	1000	2.5
NA-Hist-GCM	r5	r10	18.14°N, 26.25°W	19 September 1986	237	5.0
NA-Fut-GCM	r5	r10	18.14°N, 26.25°W	14 October 2096	268	5.0

runs that satisfied conditions 1-3 specified above. Comparison of these timeseries show that the 20-year maximum of daily precipitation (within the blue triangles) is reduced in all of the ensemble members shown. An especially strong decrease is seen in some ensemble members (e.g., r3r8 over SA in Fig. 3g) while others show weaker decreases (e.g., r5r7 over SA in Fig. 3j). Overall, the values of EPI over SAC (Fig. 4) are lower than over the other two study locations. The EPI values over NA (Fig. 5) are comparable to those over SA. However, as mentioned above, five of the NA runs we selected caused CRM crashes (black crosses in Fig. 5), and thus they are not included in our analysis below. The EPI decreases seen in the three study locations are in stark contrast with the projected EPI increases over most other regions, and thus these cases are suitable choices for further investigation of the dynamical mechanisms responsible for projected EPI decrease.

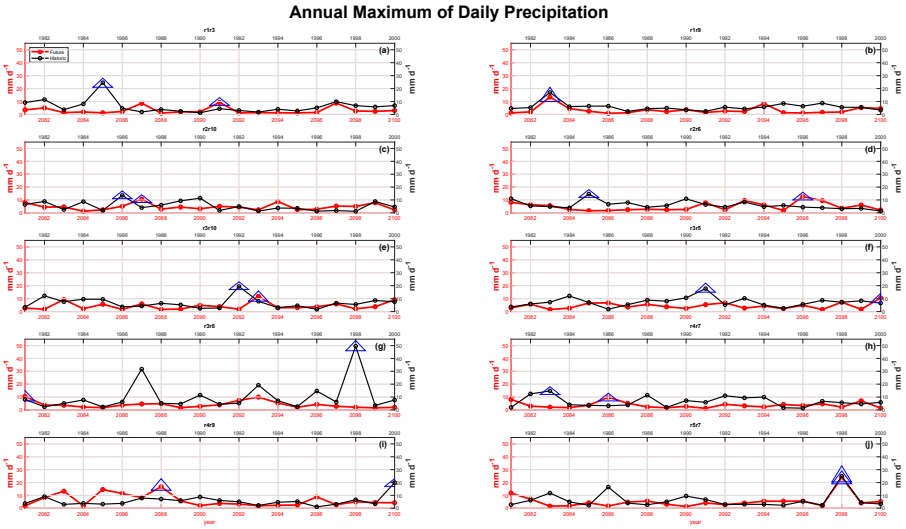

Fig. 3 Timeseries of annual maximum daily precipitation over the SA study location in CanESM2 during the historical period (1981-2000, black) and future period (2081-2100, red). Indicated above each panel is the ensemble group number followed by the ensemble member number. The blue triangles enclose the 20-year maximum events chosen for our CRM experiments. The runs shown are all of the CanESM2 runs whose large-scale forcings were used for our CRM experiments. See the text for additional details.

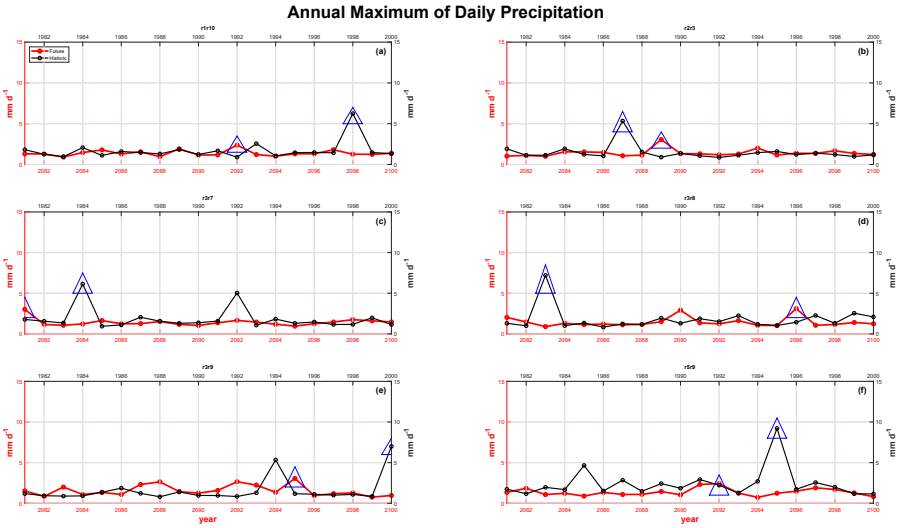

Fig. 4 As in Fig. 3 for the SAC study location.

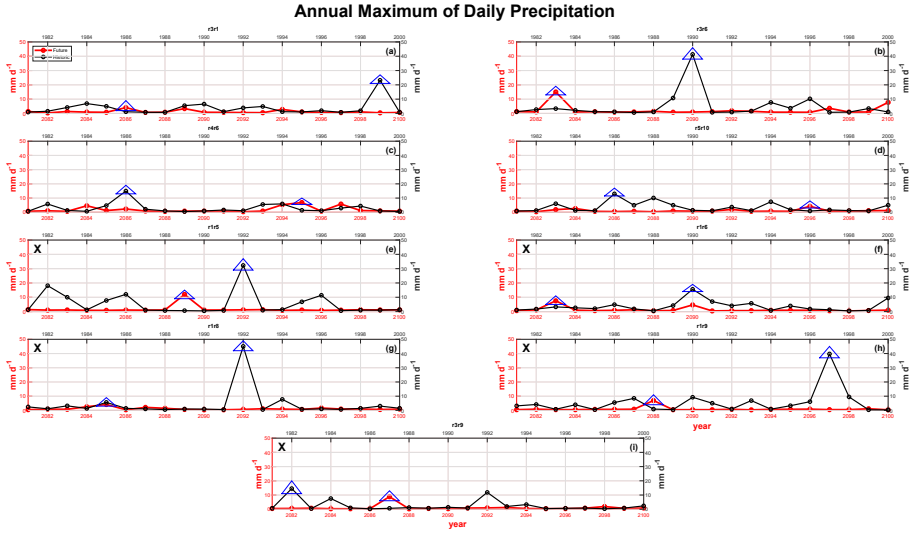

Fig. 5 As in Fig. 3 for the NA study location. The black crosses in panels e-i indicate runs that are not included in our analysis hereafter because the forcings derived from these CanESM2 runs produced numerical instability in the CRM.

Using the CanESM2 forcing fields derived as described in Section 3.2, we run the CRM for both the historical and future cases. For each GCM case identified in Table 1, a corresponding CRM experiment is performed. In each case, we run the model

for 10 days with only the temperature and moisture profiles applied, which allows the CRM to reach a state of radiative-convective equilibrium. Thereafter, the additional CQG forcings [Adv(ζ), Adv(T), Adv(q)] are turned on, beginning 15 days before the EPE and continuing until 15 days after the EPE.

4 Results and Discussion

Table 2 Ensemble mean results of the CanESM2 and CRM simulations examined in this study.

Historical Case	**Future Case**	P_E **(Hist)** [mm d^{-1}]	P_E **(Fut)** [mm d^{-1}]	$\delta P_E/P_{E0}$ [%]	δT_{sE} [K]	$\delta P_E/P_{E0}/\delta T_{sE}$ [% K^{-1}]
SA-Hist-GCM	SA-Fut-GCM	21.59	12.92	-40.16	3.8	-10.56
SA-Hist	SA-Fut	53.3	38.05	-28.61	3.8	-7.53
SA-Hist	SA-ΔL	53.3	58.64	10.1	3.8	6.3
SA-Hist	SA-ΔStab	53.3	68.58	28.67	3.8	7.54
SA-Hist	SA-ΔAdv	53.3	23.69	-55.55	3.8	-14.62
SAC-Hist-GCM	SAC-Fut-GCM	6.85	2.83	-56.69	2.41	-23.52
SAC-Hist	SAC-Fut	26.89	31.49	17.11	2.41	7.09
SAC-Hist	SAC-ΔL	26.89	26.78	-0.01	2.41	-0.00
SAC-Hist	SAC-ΔStab	26.89	28.43	5.73	2.41	2.38
SAC-Hist	SAC-ΔAdv	26.89	23.2	-13.72	2.41	-5.69
NA-Hist-GCM	NA-Fut-GCM	21.1	7.55	-64.23	3.2	-20.07
NA-Hist	NA-Fut	43.91	12.31	-71.97	3.2	-22.49
NA-Hist	NA-ΔL	43.91	51.01	16.17	3.2	5.05
NA-Hist	NA-ΔStab	43.91	44.43	1.18	3.2	0.37
NA-Hist	NA-ΔAdv	43.91	7.34	-83.28	3.2	-26.3

4.1 Model Evaluation

Having identified the cases of interest from the GCM, simulations have been performed to assess how well the CRM reproduces the selected cases. Our analysis focuses on ensemble averages of the output of our CRM experiments, as such ensemble averages reduce the noise associated with internal variability. (Hereafter, we use

"ensemble average" to refer to averages over just the CRM experiments and the associated runs of CanESM2, as described in section 3.4, rather than averages over the full CanESM2 large ensemble.) Figs. 6-8 show the comparison between the ensemble mean CRM cases (red) and the corresponding GCM cases (blue) for the historical (panel a) and future (panel b) periods in the three study locations. (See also Table 2 for precise numerical values.) All of the CRM precipitation presented in this study is horizontally averaged over the CRM domain. Quantitatively, the CRM precipitation exceeds the GCM precipitation in both the historical and future simulations. The precise reasons for the quantitative EPI differences between CanESM2 and the CRM require further investigation.

Despite these quantitative differences, the CRM qualitatively captures the decrease in EPI between the historical and future periods in the SA (Fig. 6) and NA (Fig. 8) study locations. Interestingly, the CRM produces an increase in EPI over the SAC location, in contrast with the projected decrease in CanESM2 (Fig. 7). This result suggests that the GCM-projected EPI decrease over SAC may be sensitive to the parameterization of convection, a matter worthy of further investigation in future studies. Despite this disagreement, our analysis below will provide evidence of the physical processes that are likely responsible for the GCM-projected EPI decreases over all three study locations.

Further examining individual ensemble members, we found that the peak precipitation in some CRM experiments occurred one day earlier than in the GCM. Such a difference in timing is not surprising, as the GCM parameterizes convection whereas the CRM explicitly resolves convection. Khairoutdinov and Randall (2003) also noted a precipitation timing mismatch of approximately one day when evaluating SAM against observations. Our focus in this study is on EPI rather than the precise timing of EPEs. Thus, to facilitate comparison of EPI across different experiments, we have shifted the CRM timeseries if necessary so that the timing of maximum precipitation matches that of CanESM2. This time shifting is performed prior to taking ensemble averages.

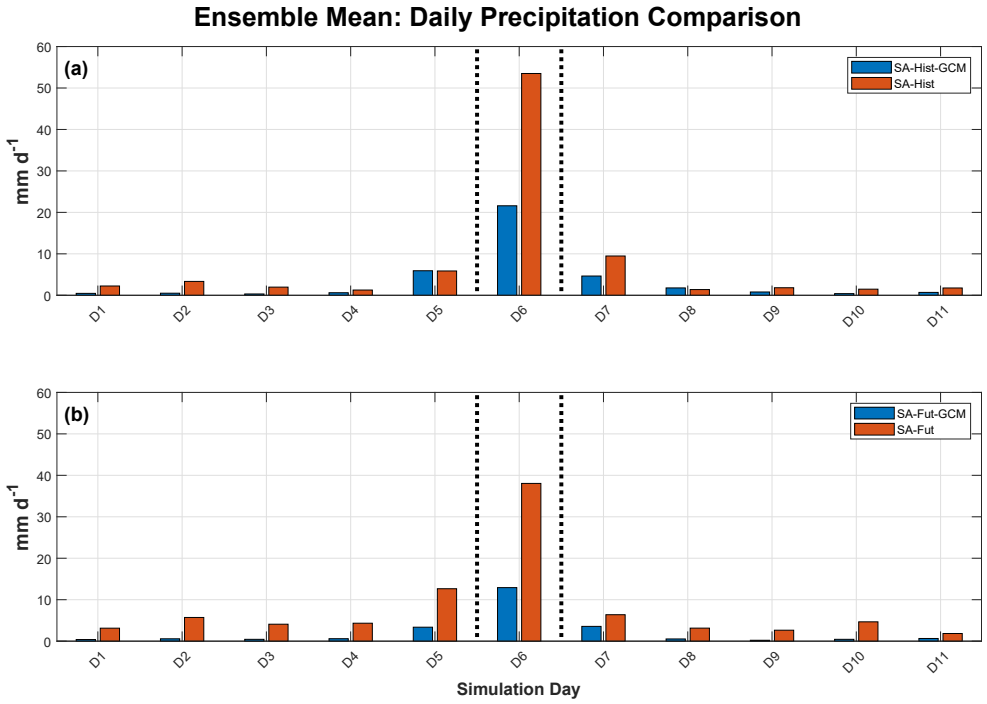

Fig. 6 Ensemble mean comparison of the CanESM2 (blue) and CRM (red) daily precipitation timeseries for the 11-day periods centered around the 20-year maxima of extreme precipitation ("simulation day 6," between the vertical dotted lines) over the SA study location during the (a) historical period and (b) future period. In this and subsequent figures, some CRM timeseries have been time shifted by 1 day prior to ensemble averaging so that the day of maximum precipitation aligns with that in the GCM runs.

4.2 Isolation Runs

To investigate the mechanisms responsible for the changes in EPI, we have performed "isolation runs" in which a subset of the CRM's large-scale forcings were taken from future projections while all other forcings were derived from historical simulations. In other words, in each isolation run, we have applied a climatic change to only a subset of the large-scale CRM forcings, while holding all other large-scale forcings fixed to those used in the historical simulations. In doing so, we isolate the effect of changes in just one or a few of the large-scale forcings.

We first consider the effect of changing just the eddy length. (See Section 3.3 for details on how eddy length is computed.) Fig. 9a shows the comparison over the SA

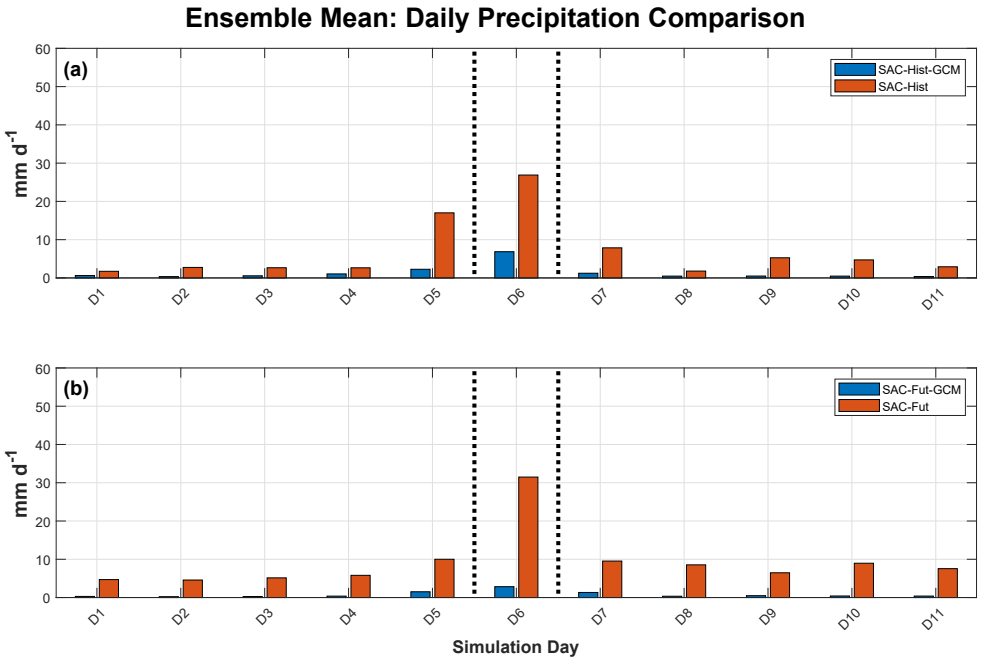

Fig. 7 As in Fig. 6 for the SAC study location.

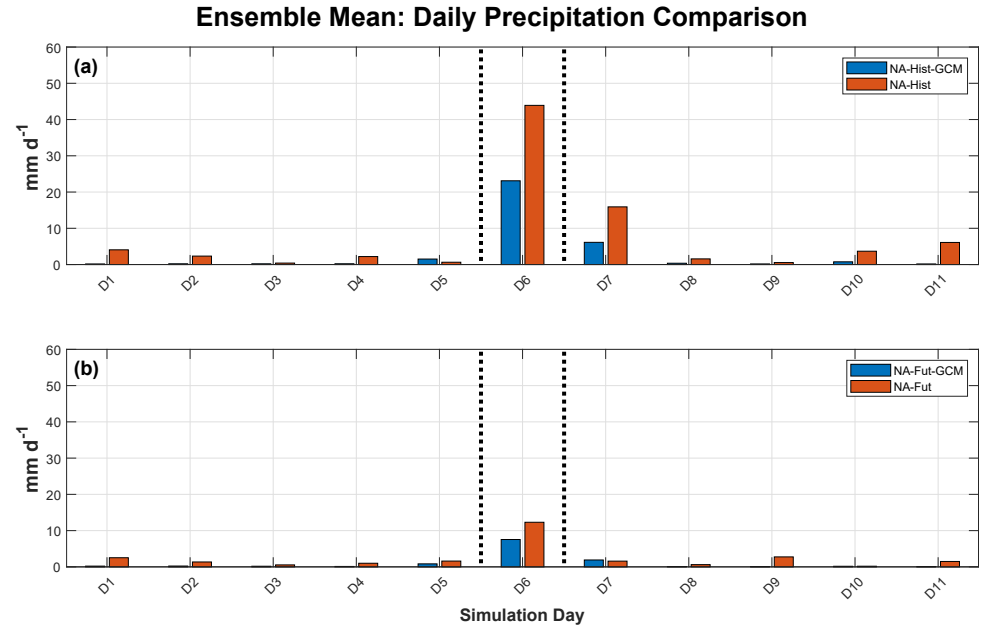

Fig. 8 As in Fig. 6 for the NA study location.

location of the eddy length isolation run SA-ΔL (yellow) with the SA-Hist (blue) and SA-Fut (red) simulations of the CRM. This experiment shows that the increase in eddy length alone causes an increase in EPI. (See also Table 2.) Over the NA location (Fig. 11a) there is also an EPI increase associated with increasing eddy length. Over the SAC location, however, eddy length increase produces a very slight decrease in EPI (Fig. 10a and Table 2).

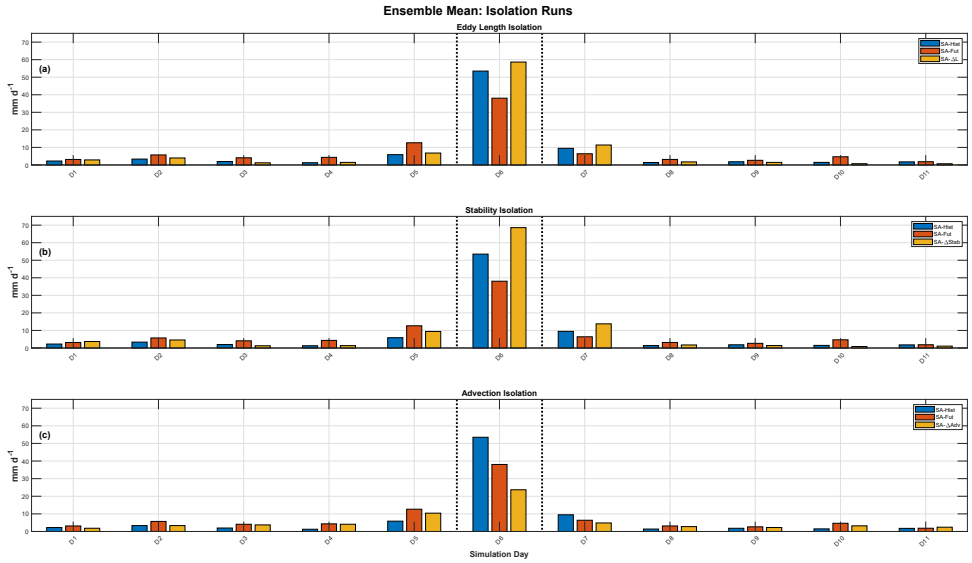

Fig. 9 Comparison of ensemble mean daily precipitation timeseries for various CRM isolation runs over the SA location. (a) SA-Hist (blue), SA-Fut (red) and SA-ΔL, isolating the eddy length effect (yellow). (b) SA-Hist (blue), SA-Fut (red) and SA-ΔStab, isolating the effects of surface temperature and vertical stability (yellow). (c) SA-Hist (blue), SA-Fut (red) and SA-ΔAdv, isolating the effect of horizontal advection (yellow). The day of extreme precipitation in CanESM2 (day 6) lies between the vertical dotted lines.

Thus, depending on the location, eddy length increase appears to have different effects. Over the SA and NA locations, eddy length increase drives an increase in EPI, indicating that the advective timescale effect is dominant, in contrast with Tandon et al (2018b). Over the SAC location, however, increasing EPI causes a decrease in EPI, indicating that the convective coupling effect is dominant, in agreement with Tandon et al (2018b). (See section 2 for additional background on the advective timescale and convective coupling effects.)

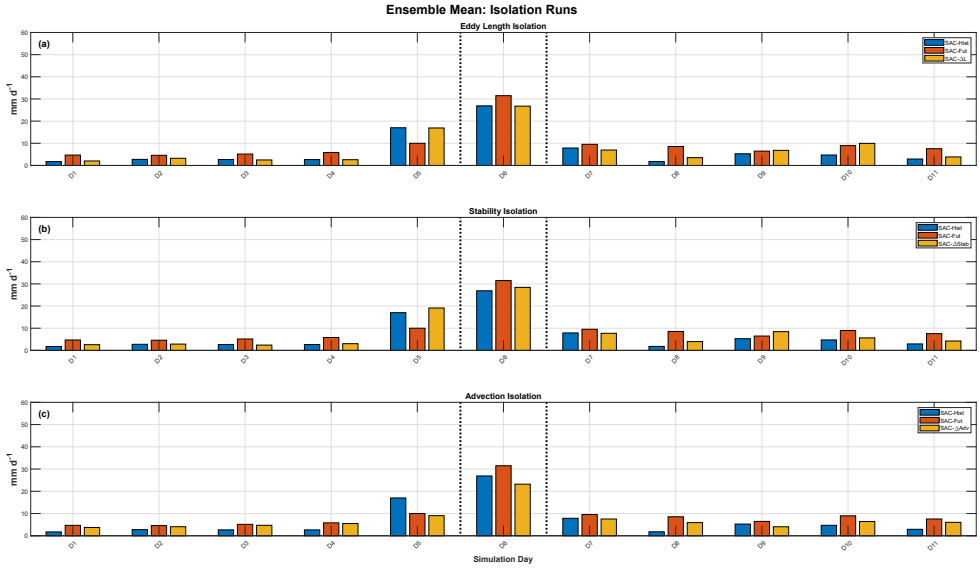

Fig. 10 As in Fig. 9 but over the SAC study location.

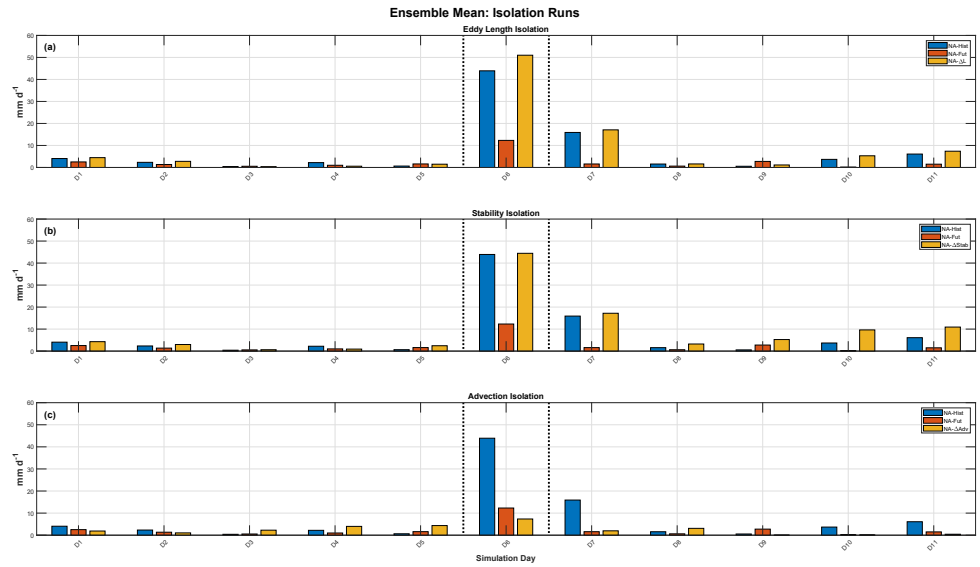

Fig. 11 As in Fig. 9 but over the NA study location.

Next we consider the effect of changing only surface temperature and vertical stability. Over the SA location (Fig. 9b), the SA-ΔStab run (yellow) produces an increase in EPI, in contrast with the EPI decrease produced when all forcings are changed (red). Over the SAC and NA locations, (Figs. 10b and 11b), the SAC-ΔStab and NA-ΔStab runs also produce increases in EPI, although the increases are very small compared to that of SA-ΔStab. (See also Table 2.) Thus, changes in surface temperature and stability likely do not explain projected decreases in EPI over the study locations. Earlier studies suggest that both stability changes and other dynamical factors may be contributing to projected EPI decreases in the subtropics (e.g., Nie et al, 2020; Li and O'Gorman, 2020), but our results suggest that changes in stability likely do not explain projected subtropical decreases of EPI, especially when surface temperature increases are taken into account.

Now we consider the effect of changing just the horizontal advective forcings. In these isolation experiments, we change the vorticity, temperature and moisture advection while holding all other forcings fixed. Over SA (Fig. 9c) and NA (Fig. 11c), advection changes (yellow) produce strong decreases in EPI, in contrast with the increases produced by other isolation runs. Over the SAC location (Fig. 10c), advection changes (yellow) also produce a decrease in EPI that is much stronger than the decrease in EPI due to eddy length increase (Fig. 10a). These results suggest that changes in horizontal advection are likely the dominant driver of projected EPI decreases in the subtropics.

This conclusion is sound even though (as mentioned above) the CRM produces an EPI increase over SAC when all forcings are changed, rather than the EPI decrease produced by the GCM (Fig. 7). The CRM explicitly resolves convection, which may cause the model to be more sensitive to surface temperature increase compared to the GCM, which may explain why the CRM produces an EPI increase when all forcings are changed. The detailed effects of convective parameterization require further investigation. This contrast notwithstanding, the CRM isolation runs over SAC agree with the runs over the other study locations in that changes in eddy length, stability and surface temperature do not produce notable decreases in EPI, but changes in horizontal advection do produce sizable decreases in EPI. Furthermore, all individual

CRM ensemble members produce EPI decreases in response to changes in horizontal advection (not shown). Thus, the subtropical EPI decreases produced by the GCM are likely due to changes in horizontal advection.

4.3 Dominant role of vorticity advection

To gain further insight, we have conducted additional experiments to isolate the effects of the individual advective forcings [Adv(ζ), Adv(q), Adv(T)]. These experiments reveal that changes in differential VA alone produce strong decreases in EPI over all three study locations (Figs. 12a, 13a, 14a). In contrast, changes in moisture advection alone produce EPI increases over all three locations (Figs. 12b, 13b, 14b). Furthermore, over SAC and NA, changes in TA alone produce EPI increases (Figs. 13c, 14c), and over SA, changes in TA produce an EPI decrease that is small compared to the decrease associated with changes in differential VA (Fig. 12c). In combination with the results of our other isolation runs (Figs. 9-11), these results strongly suggest that changes in differential VA are a key driver of EPI decrease in the study locations.

This result agrees with the findings of Nie et al (2020), who conducted analysis of output from GCMs participating in CMIP5. Nie et al (2020) found substantial contributions of large-scale dry adiabatic dynamics to subtropical decreases in EPI. Their particular diagnostic for dry dynamics encompasses both horizontal advection changes as well as changes in dry vertical stability. Our results help to clarify that decreases in EPI over the subtropical Atlantic are likely driven by changes in horizontal advection rather than dry stability.

Changes in differential VA in a particular location can arise due to the direct effect of geostrophic wind changes (i.e. changes of u_g and v_g in equation 2) or due to changes in geostrophic relative vorticity (i.e. $f_0^{-1}\nabla^2\phi$ in equation 3). In reality, geostrophic wind and $\nabla^2\phi$ cannot change independently, but it is nonetheless worthwhile to examine whether EPI changes result primarily from vorticity changes or from the direct influence of geostrophic wind changes. To this end, we have performed additional CRM experiments in which we change only the geostrophic ad-

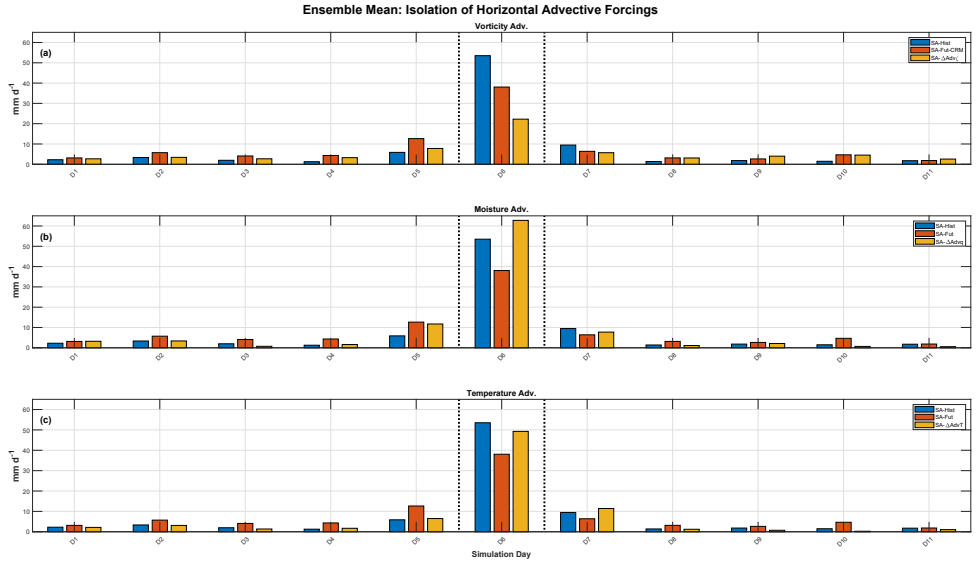

Fig. 12 Comparison of daily precipitation timeseries for CRM experiments isolating individual horizontal advective forcings over the SA location. (a) SA-Hist (blue), SA-Fut (red) and SA-ΔAdvζ, isolating the vorticity advection effect (yellow), (b) SA-Hist (blue), SA-Fut (red) and SA-ΔAdvq, isolating the moisture effect (yellow). (c) SA-Hist (blue), SA-Fut (red) and isolating the temperature advection effect (yellow). The day of the extreme precipitation in the GCM ("simulation day 6") lies between the vertical dotted lines.

vecting winds in the differential VA forcings, while leaving the geopotential and all other fields unchanged. These experiments produce a decrease in EPI over SAC (Fig. 15b), in agreement with the EPI decrease due to differential VA changes (Fig. 13c). However, these experiments produce increases in EPI over SA and NA (Fig. 15a,c), in contrast with the EPI decreases due to differential VA changes (Figs. 12c, 14c). These results suggest that, in some locations, the direct influence of geostrophic wind changes on differential VA may drive the projected EPI decrease, but in other locations, the change in the spatial structure of the geopotential field is likely the dominant driver.

To further illuminate the dynamics responsible for the EPI changes, we can linearly decompose the contributions of each large-scale forcing to ω, as detailed in section 2. Figs. 16-18 show vertical profiles of ω_ζ, ω_T and ω_Q for each CRM simulation day during the historical and future experiments over the three study locations.

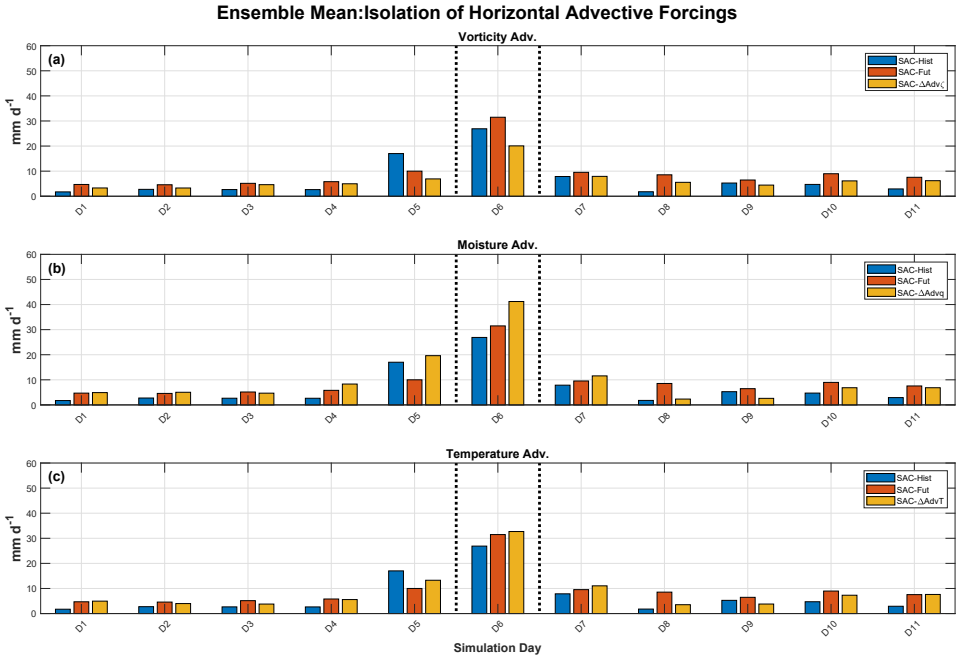

Fig. 13 As in Fig. 12 for the SAC study location.

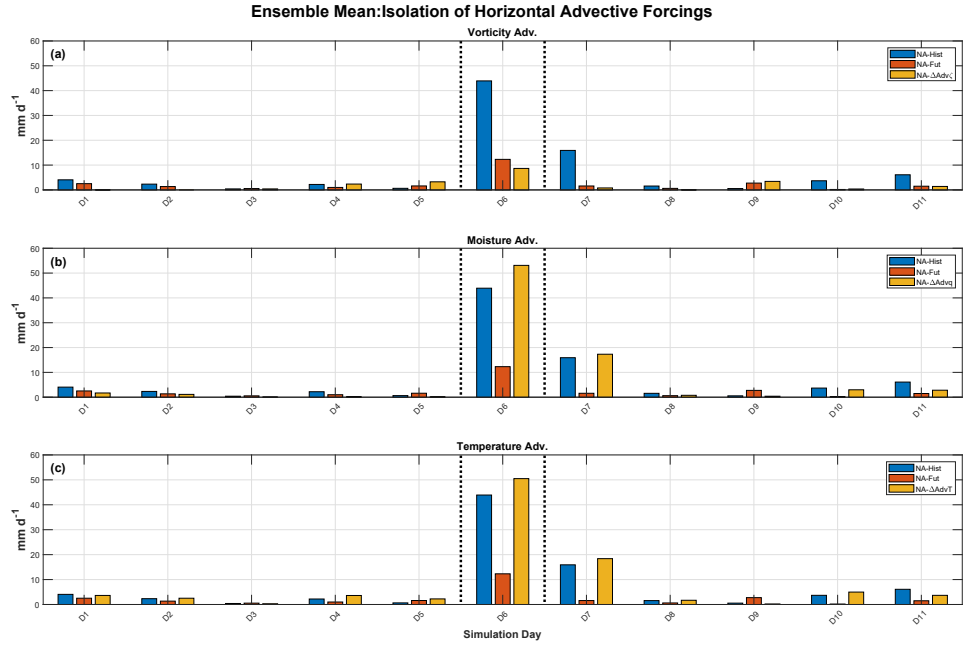

Fig. 14 As in Fig. 12 for the NA study location.

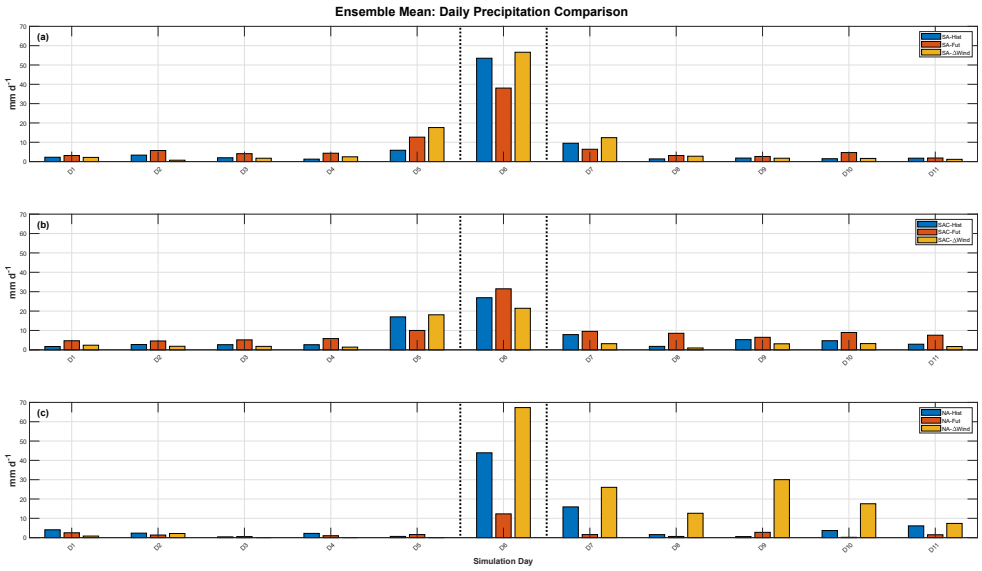

Fig. 15 Comparison of daily precipitation timeseries for CRM experiments isolating the effect of geostrophic wind changes over the three study locations. (a) SA-Hist (blue), SA-Fut (red) and SA-ΔWind, isolating the geostrophic wind effect (yellow). (b) As in (a) for the SAC study location. (c) As in (a) for the NA study location. The day of the extreme precipitation in the GCM ("simulation day 6") lies between the vertical dotted lines.

Panel a of Figs. 16-18 shows that during the EPE, ω_ζ is negative throughout the troposphere, contributing especially strong ascent in the upper troposphere. (The ascent is notably stronger over SA, Fig. 16a, compared to the other study locations.) This result reiterates the key role of differential VA in generating extreme precipitation. Furthermore, the negative ω_ζ during the future EPEs (panel b of Figs. 16-18) is much weaker compared to ω_ζ during the historical period, further establishing its role in weakening EPI. Based on the QGω equation (1), such a reduction of ω_ζ would result from $\partial_p \mathrm{Adv}(\zeta)$ becoming less negative (i.e. weaker dCVA) during the EPE. (See Section 2 for additional theoretical background.)

Comparing the first and second rows of Figs. 16-18, we see that ω_ζ is almost an order of magnitude larger than ω_T. This result may be surprising, given that in many situations, strong cancellation between ω_ζ and ω_T is expected (Trenberth, 1978). However, such cancellation depends on where within a particular wave the QGω

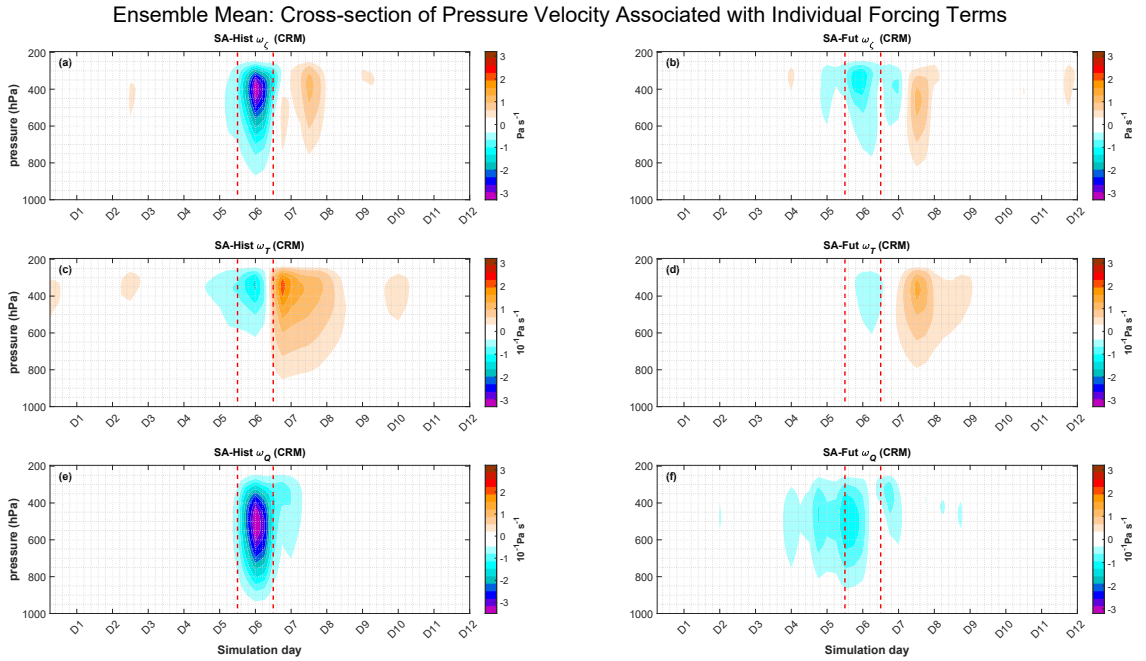

Fig. 16 Vertical pressure velocity associated with (a,b) vorticity advection, ω_ζ, (c,d) temperature advection, ω_T, and (e,f) diabatic heating, ω_Q, for the (a,c,e) SA-Hist experiments and (b,d,f) SA-Fut experiments. Red dashed lines in each panel mark the beginning and end of the day of extreme precipitation. For clarity, ω_T and ω_Q are plotted on a scale that is a factor of ten smaller than for ω_ζ.

equation is evaluated. For example, in a midlatitude wave, the region ahead of the surface cyclone but before the upper-level ridge axis is a region of both dCVA and warm air advection (WAA). Such a region exhibits unambiguous ascent forcing without cancellation between differential VA and TA.

Comparing the first and third rows of Figs. 16-18, we find that ω_ζ is also much larger than ω_Q. However, the ω_Q values are also larger than the ω_T values, so ω_Q appears to play a more significant role than ω_T. Furthermore, over all three study locations, the fractional climatic decreases of $|\omega_\zeta|$ are comparable to the fractional decreases of $|\omega_Q|$ (approximately 50% over SA, 20% over SAC and 65% over NA). This correspondence between fractional changes might explain why Tandon et al (2018b) are able to explain fractional EPI changes in terms of diabatic heating changes, without considering differential VA changes. Given that the CRM explicitly resolves con-

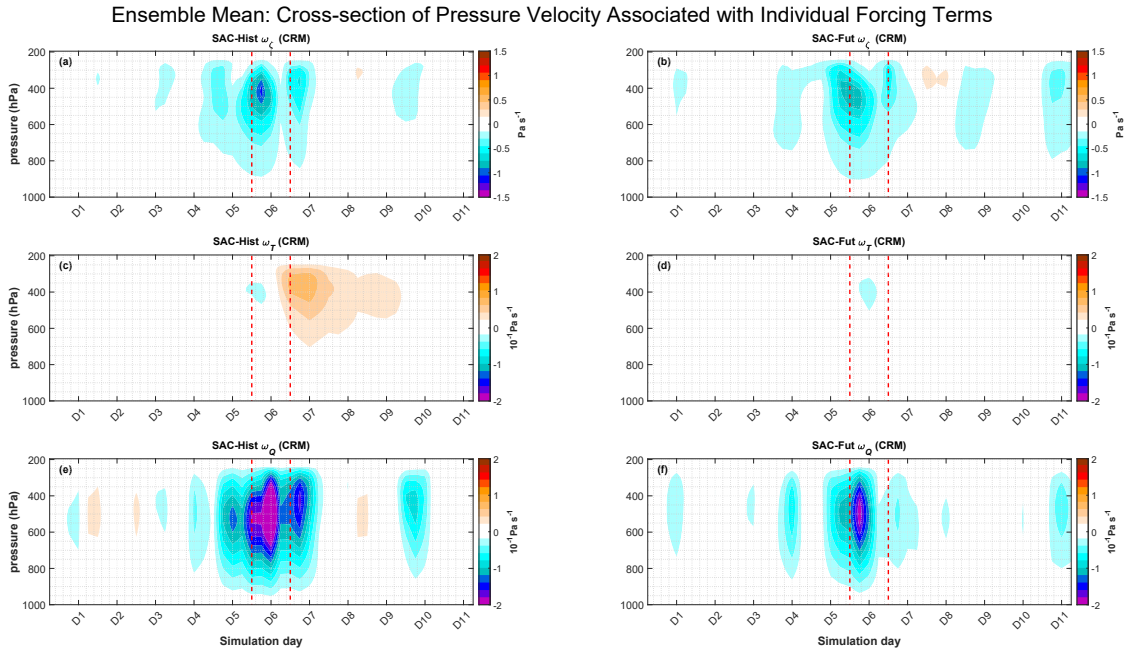

Fig. 17 As in Fig. 16 but for the SAC study location. The scales are different from those used in Fig. 16.

vection and produces quantitatively more EPI than CanESM2 (Figs. 6-8), it is possible that diabatic heating plays a stronger role in CanESM2 than in the CRM. We will investigate this possibility further in future studies. As for the current study, our results reveal that changes in differential VA are another potentially important driver of EPI changes that should be considered.

4.4 Role of large-scale circulation changes

Our results above raise the question: what is responsible for these large changes in differential VA? This question motivates additional analysis of the vertical velocity in CanESM2 during the EPEs of interest. Fig. 19 shows the vertical profiles of extreme ascent over the three study locations horizontally averaged over the CRM domain (blue) compared with the CanESM2 profiles (green) averaged over the same ensemble members used to force the CRM experiments. The maximum of $|\omega|$ is smaller in CanESM2 than in the CRM, except in NA-Fut, for which vertical velocity is generally

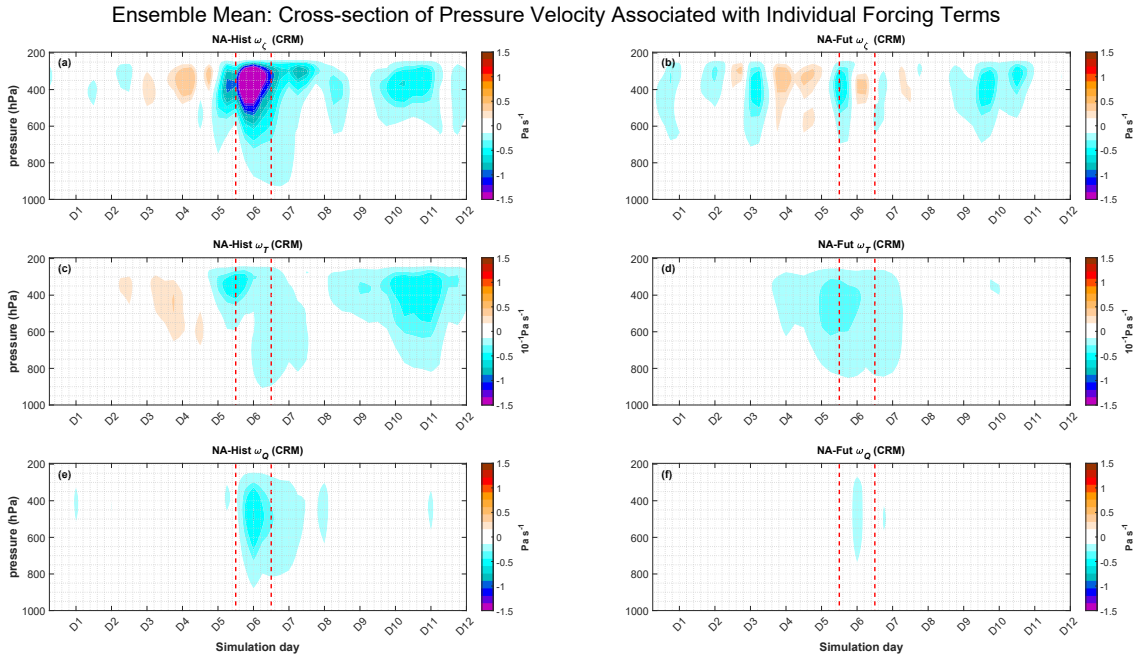

Fig. 18 As in Fig. 16 but for the NA study location. For clarity, panels c and d are plotted on a different scale from the other panels. The scales are different from those used in Fig. 16.

small. This contrast corresponds with the fact that EPI in the CRM is also greater than in CanESM2 (Figs. 6-8), the reasons for which, as discussed above, require further investigation.

Fig. 19 also shows that peak ascent in the CRM occurs higher in the troposphere than in CanESM2. This contrast is expected since frictional drag on horizontal wind as well as the impenetrable solid Earth constrain both ω and $\partial\omega/\partial p$ to be near-zero at the surface. (At the top of the troposphere, there is also a constraint on ω, but no constraint on $\partial\omega/\partial p$.) Thus, a stronger maximum $|\omega|$ typically occurs higher in the troposphere. This correspondence is also evident when comparing historical and future profiles of ω: compared to peak $|\omega|$ in the historical period, peak $|\omega|$ in the future period is generally smaller and occurs lower in the troposphere.

Interestingly, peak $|\omega|$ in the CRM also decreases slightly over SAC, even though the CRM produces an EPI increase in this location (Fig. 7). This result suggests that the EPI increase in the CRM may be due to increases in column moisture that over-

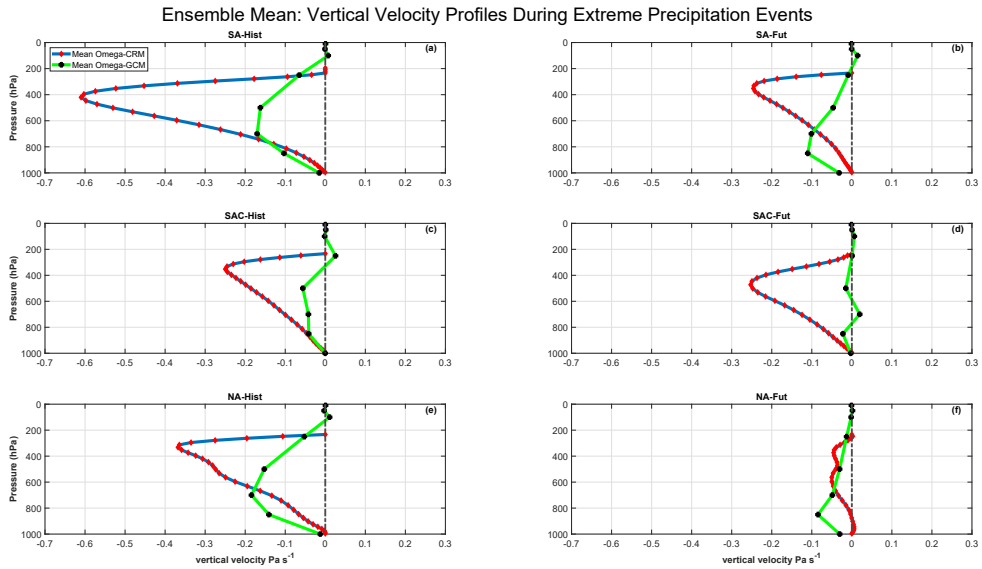

Fig. 19 Ensemble mean, daily mean vertical pressure velocity profiles on the day of extreme precipitation in the (a) SA-Hist, (b) SA-Fut, (c) SAC-Hist, (d) SAC-Fut, (e) NA-Hist and (f) NA-Fut cases for the CRM (blue lines with red dots) and the GCM (green lines with black dots).

compensate for the weaker ascent. The influence of convective parameterization on the column moisture changes require further investigation. Altogether, the CanESM2 ω profiles in Fig. 19 reveal, as expected, clear climatic weakening of large-scale extreme ascent, which is responsible for the decreased EPI in all three study locations. Such weakening of large-scale ascent suggests a possible influence of other large-scale circulation changes that might explain the changes in differential VA.

One possibility to consider is whether changes in differential VA arise from spatial shifts in the large-scale atmospheric circulation. As the atmosphere warms, key features of the large-scale circulation, in particular the midlatitude jets and Hadley Cell edges, are expected to shift poleward (e.g., Lu et al, 2008; Seidel et al, 2008; Johanson and Fu, 2009; Tandon et al, 2013). Earlier studies have suggested that such spatial shifts in the Hadley Cell edges might partly explain subtropical decreases in EPI (Pfahl et al, 2017; Norris et al, 2020). Figure 20 shows the spatial structure of the CanESM2 ω and P fields during the EPEs of interest. Comparing the left and right columns, we see a clear weakening of extreme ascent, as we did in Fig. 19. However,

such changes in vertical velocity do not appear to arise from a spatial shift of the ω field. For example, the ω field in SA-Hist-GCM (Figure 20a) shows peak ascending values slightly east of the study location and weaker ascent in the surrounding regions. One could envision this ω field shifting south with the expected poleward expansion of the Hadley circulation (e.g., Lu et al, 2008; Seidel et al, 2008; Johanson and Fu, 2009; Tandon et al, 2013), which would result in weaker ascent at the study location. However, there is no clear indication of a corresponding shift in the ω field, and instead, the ω field appears to shift slightly to the northwest (i.e. equatorward, Fig. 20b). Even that shift, however, cannot explain the weakening of ascent at the study location, as the peak ascent in the future period sits over the study location, but the peak ascent is about 50% weaker than during the historical period. Overall, the ascent at the study location appears to weaken independently of any spatial shift of the ω field. We reach the same conclusion when examining ω changes at the other study locations (Fig. 20c-f): the weakening of ascent cannot be explained in terms of a simple spatial shift of the ω field. Over SAC (Fig. 20c-d), there is some indication of a southward shift of the ω field, but again, the magnitude of the ω change at the study location cannot be explained primarily by a spatial shift of the ω field. Over NA (Fig. 20e-f), There is no clear indication of a spatial shift in the ω field. It is still possible that a spatial shift of the Hadley Cell edges plays a key role in these changes. But if Hadley Cell edge shifts play such a role, it does not appear to manifest as a simple spatial shift of the ω field during EPEs, and the precise means by which the Hadley Cell edges might influence the extreme ascent field requires further investigation.

These results suggest that factors other than spatial circulation shifts may be responsible for the changes in ω and differential VA. One possible explanation arises from considering the change in layer thickness as the atmosphere warms. Neglecting the effect of moisture on the gas constant, we can express hydrostatic balance as

$$\frac{\partial \phi}{\partial \ln p} = -RT. \tag{6}$$

Thus, an increase in temperature produces an increase in spacing between geopotential surfaces. It is conceivable that such an increase in layer thickness is horizontally uniform, in which case there might be no impact on differential VA. However, mass

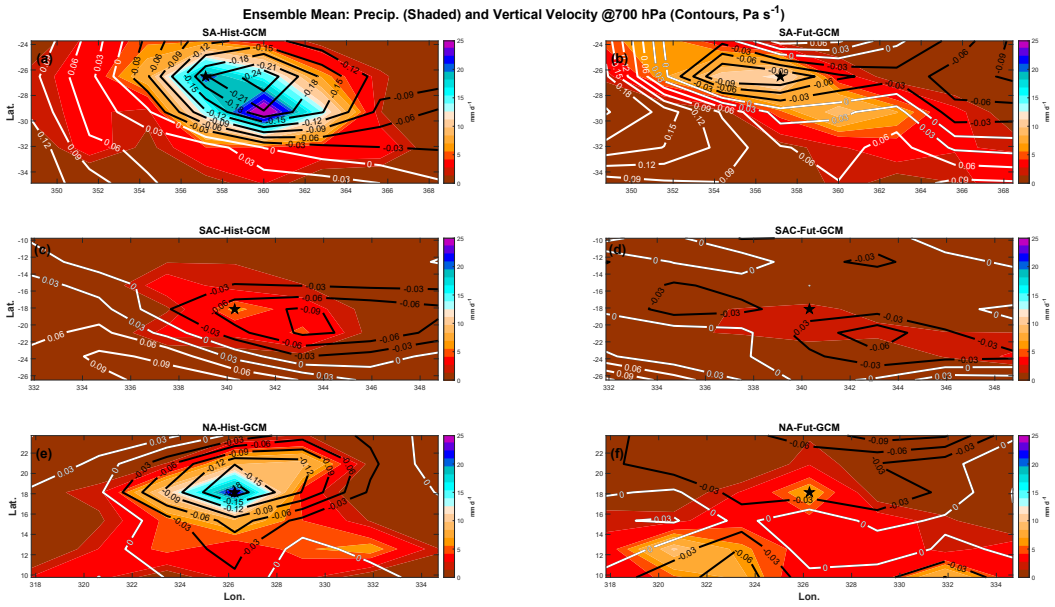

Fig. 20 CanESM2 precipitation (shading) and ω at 700 hPa (contours) during EPEs over the (a,b) SA, (c,d) SAC and (e,f) NA study locations during the (a,c,e) historical and (b,d,f) future periods. Negative contours are black and nonnegative contours are white with a contour interval of 0.03 Pa s^{-1}. The black stars indicate the study locations. The fields have been averaged over the same ensemble members used for the CRM experiments.

conservation would prevent a globally uniform decrease in ascent. Therefore, changes in ω with warming must be spatially non-uniform, which requires that the horizontal curvature of geopotential surfaces must change as well.

Thus, an increase in layer thickness requires that the curvature of geopotential surfaces must change. In particular, the positive curvature of geopotential surfaces must decrease more at upper levels than at lower levels. These changes in turn require the circulation to advect geopotential disturbances whose positive curvature is reduced more at upper levels compared to lower levels, which implies a greater reduction in cyclonic vorticity at upper levels compared to lower levels (i.e. weaker dCVA), which in turn implies weaker ascent. Additional work is needed to determine whether such a mechanism is responsible for changes in dCVA during EPEs.

Our key point here is that it is possible that weakening of dCVA (which is the dominant driver of decreased EPI in our CRM experiments) is just a natural conse-

quence of warming, and changes in this aspect of the large-scale circulation do not necessarily require a spatial shift in the large-scale circulation. As stated above, spatial shifts of the large-scale mean circulation might still contribute to dCVA changes, and additional work is needed to determine the mechanism primarily responsible for dCVA changes.

5 Summary and Conclusion

We have conducted dynamical downscaling experiments using a CRM driven by CanESM2 output in order to examine the dynamical mechanisms influencing projected subtropical decreases of EPI. In two of the three study locations (SA and NA), the CRM produces an ensemble mean decrease in EPI over the subtropical South Atlantic Ocean and subtropical North Atlantic that is in qualitative agreement with CanESM2 projections. In one of the study locations (SAC), the CRM produces an EPI increase, in contrast with the decrease produced in CanESM2. Nonetheless, when individual forcings are varied in isolation, CRM experiments over all three study locations reveal that weakening of dCVA is the dominant driver of decreased EPI. Weakening of dCVA indicates that there is a decrease in the amount by which VA at upper levels exceeds VA at lower levels.

The precise reason for the decreases in dCVA require further investigation. One possibility that we outline is that the increase in layer thicknesses with warming require geopotential curvature to change in such a way that cyclonic VA is reduced at upper levels compared to lower levels. Another possibility is that spatial shifts of the mean circulation (associated with Hadley cell expansion) somehow influence the ω field during EPEs. We find that the extreme ascent fields do not appear to shift spatially in a way that resembles spatial shifts of the mean circulation (Fig. 20), but it is possible that mean circulation spatial shifts influence the extreme ascent field in other ways that we have not considered.

In our CRM experiments, vertical stability changes are not the dominant driver of projected decreases in EPI. When vertical stability and surface temperature changes are imposed without changes in other forcings, they produce EPI increases rather

than decreases over all three study locations. This finding helps to clarify the results of Nie et al (2020), which allowed for the possibility that vertical stability changes contribute to projected decreases of EPI in some subtropical locations.

Our CRM experiments also suggest that eddy length changes are not a dominant driver of subtropical EPI decreases, in contrast with the analysis of Tandon et al (2018b). However, the eddy length parameterization we use is not applied to the geostrophic vorticity field that drives the CRM. That is, we explicitly compute the Laplacian of the geopotential from the GCM, instead of treating it as a wave-like disturbance in terms of the eddy length. Given the importance of vorticity changes, it is possible that eddy length changes would play a stronger role if their direct effect on the geostrophic vorticity were captured within the CQG framework. This is a possibility we will explore in the future.

Although the role of dCVA is clear in our CRM experiments, the CRM used in this study lacks possible stabilizing feedbacks between large-scale vertical velocity and horizontal advection, and it may also have high sensitivity to large-scale forcings compared to CanESM2. Furthermore, as discussed in section 3.3, we had to apply adjustment factors to the CanESM2-derived eddy length in order to maintain numerical stability in our CRM experiments. So the mechanisms of EPI change found in our CRM experiments may not fully reflect mechanisms in GCMs, and this is a topic in need of further investigation. Nonetheless, our results do highlight a clear dynamical mechanism of possible importance to future changes in EPI. Given the established role of VA in observed subtropical EPEs (e.g., de Vries et al, 2018; Ma et al, 2019; de Vries, 2021), our results motivate further examination of its role in future EPI changes. With additional controlled modelling experiments over a variety of regions (especially over land regions and the Pacific Ocean, which we have not considered here), we aim to build up a level of mechanistic understanding that can be used to further assess climate models and improve confidence in regional projections of extreme precipitation.

Acknowledgements Support for this research was provided by Contract 300697135 from Environment and Climate Change Canada (ECCC) and a Discovery Grant from the Natural Sciences and Engineering

Research Council of Canada (NSERC). We acknowledge Megan Kirchmeier-Young in her role as scientific authority for the ECCC contract. We thank Ji Nie for helpful discussions and assistance with the CQG framework, and we thank Marat Khairoutdinov for further assistance with compiling SAM. Devanarayana Rao provided generous assistance with MATLAB coding. Gary Klaassen, Yongsheng Chen and Rashid Bashir provided valuable feedback on an earlier version of this manuscript. Two anonymous reviewers provided constructive feedback on the submitted manuscript. Guilong Li and Yanjun Jiao at ECCC generously assisted with obtaining CanESM2 output. Output from the CanESM2 Large Ensemble can be obtained from `https://open.canada.ca/data/en/dataset/aa7b6823-fd1e-49ff-a6fb-68076a4a477c`. The CRM simulations presented in this study were performed on Compute Canada's graham and cedar high-performance computing clusters.

References

Alexander LV, Zhang X, Peterson TC, Caesar J, Gleason B, Klein Tank AMG, Haylock M, Collins D, Trewin B, Rahimzadeh F, Tagipour A, Rupa Kumar K, Revadekar J, Griffiths G, Vincent L, Stephenson DB, Burn J, Aguilar E, Brunet M, Taylor M, New M, Zhai P, Rusticucci M, Vazquez-Aguirre JL (2006) Global observed changes in daily climate extremes of temperature and precipitation. Journal of Geophysical Research: Atmospheres 111(D5), DOI https://doi.org/10.1029/2005JD006290

Arora VK, Scinocca JF, Boer GJ, Christian JR, Denman KL, Flato GM, Kharin VV, Lee WG, Merryfield WJ (2011) Carbon emission limits required to satisfy future representative concentration pathways of greenhouse gases. Geophysical Research Letters 38(5), DOI https://doi.org/10.1029/2010GL046270

Bao J, Sherwood SC, Colin M, Dixit V (2017) The robust relationship between extreme precipitation and convective organization in idealized numerical modeling simulations. Journal of Advances in Modeling Earth Systems 9(6):2291–2303, DOI https://doi.org/10.1002/2017MS001125

Brönnimann S, Rajczak J, Fischer EM, Raible CC, Rohrer M, Schär C (2018) Changing seasonality of moderate and extreme precipitation events in the Alps. Natural Hazards and Earth System Sciences 18(7):2047–2056, DOI https://doi.org/10.5194/nhess-18-2047-2018

Coppola E, Sobolowski S, Pichelli E, Raffaele F, Ahrens B, Anders I, Ban N, Bastin S, Belda M, Belusic D, Caldas-Alvarez A, Cardoso RM, Davolio S, Dobler A, Fernandez J, Fita L, Fumiere Q, Giorgi F, Goergen K, Güttler I, Halenka T, Heinzeller D, Hodnebrog Ø, Jacob D, Kartsios S, Katragkou E, Kendon E, Khodayar S, Kunstmann H, Knist S, Lavín-Gullón A, Lind P, Lorenz T, Maraun D, Marelle L, van Meijgaard E, Milovac J, Myhre G, Panitz HJ, Piazza M, Raffa M, Raub T, Rockel B, Schär C, Sieck K, Soares PMM, Somot S, Srnec L, Stocchi P, Tölle MH, Truhetz H, Vautard R, de Vries H, Warrach-Sagi K (2020) A first-of-its-kind multi-model convection permitting ensemble for investigating convective phenomena over Europe and the Mediterranean. Climate Dyn 55:3–34, DOI 10.1007/s00382-018-4521-8

Dai P, Nie J (2020) A global quasigeostrophic diagnosis of extratropical extreme precipitation. Journal of Climate 33(22):9629 – 9642, DOI https://doi.org/10.1175/JCLI-D-20-0146.1

Dwyer JG, O'Gorman PA (2017) Changing duration and spatial extent of midlatitude precipitation extremes across different climates. Geophysical Research Letters 44(11):5863–5871, DOI https://doi.org/10.1002/2017GL072855

Hegdahl TJ, Engeland K, M?ller M, Sillmann J (2020) An event-based approach to explore selected present and future atmospheric river–induced floods in western Norway. J Hydrometeor 21:2003 – 2021, DOI 10.1175/JHM-D-19-0071.1

Holton JR, Hakim GJ (2012) An Introduction to Dynamic Meteorology, 5th edn. Elsevier

Huffman GJ, Adler RF, Arkin P, Chang A, Ferraro R, Gruber A, Janowiak J, McNab A, Rudolf B, Schneider U (1997) The global precipitation climatology project GPCP combined precipitation dataset. Bulletin of the American Meteorological Society 78(1):5–20, DOI https://doi.org/10.1175/1520-0477(1997)078⟨0005:TGPCPG⟩2.0.CO;2

Johanson CM, Fu Q (2009) Hadley cell widening: model simulations versus observations. J Climate 22:2713–2725, DOI 10.1175/2008JCLI2620.1

Khairoutdinov MF, Randall DA (2003) Cloud resolving modeling of the ARM summer 1997 IOP: Model formulation, results, uncertainties, and sensitivities. Jour-

832 nal of the Atmospheric Sciences 60(4):607–625, DOI https://doi.org/10.1175/
833 1520-0469(2003)060⟨0607:CRMOTA⟩2.0.CO;2
834 Kidston J, Dean SM, Renwick JA, Vallis GK (2010) A robust increase in the eddy
835 length scale in the simulation of future climates. Geophysical Research Letters
836 37(3):n/a–n/a, DOI https://doi.org/10.1029/2009GL041615
837 Kronstadt KA, Pervaze AS, Vaughn B (2011) Flooding in Pakistan: Overview and
838 issues for congress. environmental stress in Pakistan and U.S. interests. Internet,
839 URL https://www.everycrsreport.com/reports/R40926.html
840 Li Z, O'Gorman PA (2020) Response of vertical velocities in extratropical precipi-
841 tation extremes to climate change. Journal of Climate 33(16):7125 – 7139, DOI
842 https://doi.org/10.1175/JCLI-D-19-0766.1
843 Liu C, Ikeda K, Rasmussen R, Barlage M, Newman AJ, Prein AF, Chen F, Chen L,
844 Clark M, Dai A, Dudhia J, Eidhammer T, Gochis D, Gutmann E, Kurkute S, Li Y,
845 Thompson G, Yates D (2017) Continental-scale convection-permitting modeling
846 of the current and future climate of North America. Climate Dyn 49:71–95, DOI
847 10.1007/s00382-016-3327-9
848 Lu J, Chen G, Frierson DMW (2008) Response of the zonal mean atmospheric
849 circulation to El Niño versus global warming. J Climate 21:5835–5851, DOI
850 10.1175/2008JCLI2200.1
851 Ma T, Wu G, Liu Y, Jiang Z, Yu J (2019) Impact of surface potential vorticity density
852 forcing over the Tibetan Plateau on the South China extreme precipitation in Jan-
853 uary 2008. Part I: Data analysis. Journal of Meteorological Research 33(3):400–
854 415
855 Marelle L, Myhre G, Hodnebrog Ø, Sillmann J, Samset BH (2018) The changing
856 seasonality of extreme daily precipitation. Geophysical Research Letters 45(20),
857 DOI https://doi.org/10.1029/2018GL079567
858 Masson-Delmotte V, Zhai P, Pörtner HO, Roberts D, Skea J, Shukla PR, Pirani A,
859 Moufouma-Okia W, Péan C, Pidcock R, et al (2018) IPCC, 2018: Summary for
860 policymakers. In: Global warming of 1.5°C. an IPCC Special Report on the im-
861 pacts of global warming of 1.5°C above pre-industrial levels and related global
862 greenhouse gas emission pathways,in the context of strengthening the global re-

sponse to the threat of climate change, sustainable development,and efforts to eradicate poverty. URL https://www.ipcc.ch/sr15/chapter/spm/

Milrad SM, Lombardo K, Atallah EH, Gyakum JR (2017) Numerical simulations of the 2013 Alberta flood: Dynamics, thermodynamics, and the role of orography. Monthly Weather Review 145(8):3049–3072, DOI https://doi.org/10.1175/MWR-D-16-0336.1

Nie J, Sobel AH (2016) Modeling the interaction between quasigeostrophic vertical motion and convection in a single column. Journal of the Atmospheric Sciences 73(3):1101–1117, DOI https://doi.org/10.1175/JAS-D-15-0205.1

Nie J, Shaevitz DA, Sobel AH (2016b) Forcings and feedbacks on convection in the 2010 Pakistan flood: Modeling extreme precipitation with interactive large-scale ascent. Journal of Advances in Modeling Earth Systems 8(3):1055–1072, DOI https://doi.org/10.1002/2016MS000663

Nie J, Sobel AH, Shaevitz DA, Wang S (2018) Dynamic amplification of extreme precipitation sensitivity. Proceedings of the National Academy of Sciences 115(38):9467–9472, DOI https://doi.org/10.1073/pnas.1800357115

Nie J, Dai P, Sobel AH (2020) Dry and moist dynamics shape regional patterns of extreme precipitation sensitivity. Proceedings of the National Academy of Sciences 117(16):8757–8763, DOI https://doi.org/10.1073/pnas.1913584117

Norris J, Chen G, Li C (2020) Dynamic amplification of subtropical extreme precipitation in a warming climate. Geophysical Research Letters 47(14):e2020GL087,200, DOI https://doi.org/10.1029/2020GL087200

O'Gorman PA, Schneider T (2009a) The physical basis for increases in precipitation extremes in simulations of 21st-century climate change. Proceedings of the National Academy of Sciences 106(35):14,773–14,777, DOI https://doi.org/10.1073/pnas.0907610106

O'Gorman PA, Schneider T (2009b) Scaling of precipitation extremes over a wide range of climates simulated with an idealized GCM. Journal of Climate 22(21):5676 – 5685, DOI https://doi.org/10.1175/2009JCLI2701.1

Pendergrass AG, Lehner F, Sanderson BM, Xu Y (2015) Does extreme precipitation intensity depend on the emissions scenario? Geophysical Research Letters

894 42(20):8767–8774, DOI https://doi.org/10.1002/2015GL065854
895 Pendergrass AG, Reed KA, Medeiros B (2016) The link between extreme pre-
896 cipitation and convective organization in a warming climate: Global radiative-
897 convective equilibrium simulations. Geophysical Research Letters 43(21):11,445–
898 11,452, DOI https://doi.org/10.1002/2016GL071285
899 Pfahl S, O'Gorman PA, Fischer EM (2017) Understanding the regional pattern of pro-
900 jected future changes in extreme precipitation. Nature Climate Change 7(6):423–
901 427, DOI https://doi.org/10.1038/nclimate3287
902 Pichelli E, Coppola E, Sobolowski S, Ban N, Giorgi F, Stocchi P, Alias A, Belušić D,
903 Berthou S, Caillaud C, Cardoso RM, Chan S, Christensen OB, Dobler A, de Vries
904 H, Goergen K, Kendon EJ, Keuler K, Lenderink G, Lorenz T, Mishra AN, Panitz
905 HJ, Schär C, Soares PMM, Truhetz H, Vergara-Temprado J (2021) The first multi-
906 model ensemble of regional climate simulations at kilometer-scale resolution part
907 2: historical and future simulations of precipitation. Climate Dyn 56:3581–3602,
908 DOI 10.1007/s00382-021-05657-4
909 Pierce DW, Barnett TP, Santer BD, Gleckler PJ (2009) Selecting global climate mod-
910 els for regional climate change studies. Proceedings of the National Academy of
911 Sciences 106(21):8441–8446, DOI https://doi.org/10.1073/pnas.0900094106
912 Prein AF, Rasmussen RM, Ikeda K, Liu C, Clark MP, Holland GJ (2016) The future
913 intensification of hourly precipitation extremes. Nature Climate Change 7:48, URL
914 http://dx.doi.org/10.1038/nclimate3168
915 Rajczak J, Pall P, Schär C (2013) Projections of extreme precipitation events in re-
916 gional climate simulations for Europe and the Alpine Region. J Geophys Res At-
917 mos 118(9):3610–3626, DOI https://doi.org/10.1002/jgrd.50297
918 Randall D, Wood R, Bony S, Colman R, Fichefet T, Fyfe J, Kattsov V, Pit-
919 man A, Shukla J, Srinivasan J, Stouffer R, Sumi A, Taylor K (2007) Climate
920 change 2007: The physical science basis. contribution of Working Group I to
921 the fourth assessment report of the Intergovernmental Panel on Climate Change.
922 Internet, URL http://web.crc.losrios.edu/~larsenl/ExtraMaterials/
923 IPCC4/ar4-wg1-chapter8.pdf

Riahi K, Rao S, Krey V, Cho C, Chirkov V, Fischer G, Kindermann G, Nakicenovic N, Rafaj P (2011) RCP 8.5—a scenario of comparatively high greenhouse gas emissions. Climatic Change 109(1-2):33–57, DOI https://doi.org/10.1007/s10584-011-0149-y

Seidel DJ, Fu Q, Randel WJ, Reichler TJ (2008) Widening of the tropical belt in a changing climate. Nature Geosci 1:21–24, DOI 10.1038/ngeo.2007.38

Sobel AH, Bretherton CS (2000) Modeling tropical precipitation in a single column. J Climate 13:4378 – 4392, DOI 10.1175/1520-0442(2000)013⟨4378:MTPIAS⟩2.0.CO;2

Tandon NF, Gerber EP, Sobel AH, Polvani LM (2013) Understanding Hadley Cell expansion versus contraction: Insights from simplified models and implications for recent observations. J Climate 26:4304–4321, DOI 10.1175/JCLI-D-12-00598.1

Tandon NF, Nie J, Zhang X (2018a) Strong influence of eddy length on boreal summertime extreme precipitation projections. Geophysical Research Letters 45(19):10,665–10,672, DOI https://doi.org/10.1029/2018GL079327

Tandon NF, Zhang X, Sobel AH (2018b) Understanding the dynamics of future changes in extreme precipitation intensity. Geophysical Research Letters 45(6):2870–2878, DOI https://doi.org/10.1002/2017GL076361

Trenberth KE (1978) On the interpretation of the diagnostic quasi-geostrophic omega equation. Monthly weather review 106(1):131–137

Trenberth KE (1999) Atmospheric moisture recycling: Role of advection and local evaporation. Journal of Climate 12(5):1368–1381, DOI https://doi.org/10.1175/1520-0442(1999)012⟨1368:AMRROA⟩2.0.CO;2

Trenberth KE, Fasullo JT, Shepherd TG (2015) Attribution of climate extreme events. Nature Climate Change 5(8):725–730, DOI https://doi.org/10.1038/nclimate2657

Vaqar A, Khan MAA, Shakeel R, Zuhair M, Amir P (2011) National economic and environmental development study: The case of Pakistan. MPRA Paper 30942, University Library of Munich, Germany, URL `https://ideas.repec.org/p/pra/mprapa/30942.html`

de Vries AJ (2021) A global climatological perspective on the importance of Rossby wave breaking and intense moisture transport for extreme precipitation

955 events. Weather and Climate Dynamics 2(1):129–161, DOI https://doi.org/10.
956 5194/wcd-2-129-2021
957 de Vries AJ, Ouwersloot HG, Feldstein SB, Riemer M, El Kenawy AM, McCabe MF,
958 Lelieveld J (2018) Identification of tropical-extratropical interactions and extreme
959 precipitation events in the Middle East based on potential vorticity and moisture
960 transport. Journal of Geophysical Research: Atmospheres 123(2):861–881, DOI
961 https://doi.org/10.1002/2017JD027587
962 Westra S, Alexander LV, Zwiers FW (2013) Global increasing trends in annual
963 maximum daily precipitation. Journal of Climate 26(11):3904–3918, DOI https:
964 //doi.org/10.1175/JCLI-D-12-00502.1
965 WMO (2018) Guidelines on the defintion and monitoring of extreme weather and
966 climate events. Task team on the definition of extreme weather and climate events.
967 DOI https://doi.org/10.1109/CSCI.2015.171
968 Zheng F, Westra S, Leonard M (2015) Opposing local precipitation extremes. Nature
969 Climate Change 5(5):389–390, DOI https://doi.org/10.1038/nclimate2579